

NTSB Battery Nail Penetration Tests

Final Report for 787 Battery (Asset 436) Tested at 70°C, Ungrounded

J. Thomas Chapin, PhD
Pravinray D. Gandhi, PhD, PE
Paul W. Brazis, Jr., PhD
May 29, 2014





Final Report for 787 Battery (Asset 436) Tested at 70°C, Ungrounded

NOTICE

The issuance of this Report does not constitute an endorsement of any proposed amendment and in no way implies Listing, Classification, or other recognition by UL and does not authorize the use of UL Listing or Classification Marks or any other reference to Underwriters Laboratories Inc. on, or in connection with, the product.

UL LLC, its employees, and its agents shall not be responsible to anyone for the use or nonuse of the information contained in this Report, and shall not incur any obligation or liability for damages, including consequential damages, arising out of or in connection with the use of, or inability to use, the information contained in this Report.

Release Type	<input type="checkbox"/> Internal <input checked="" type="checkbox"/> External (Confidential) <input type="checkbox"/> External (Public)	
UL Distribution	UL Corporate Research and UL staff signed onto the Mutual Non-Disclosure Agreement with the NTSB.	
External Distribution	Release approved only to the National Transportation Safety Board (NTSB) – Release subject to Mutual Non-Disclosure Agreement (NDA).	
Date:	Keywords: NTSB, 787 battery, Li-ion battery, Nail penetration test, internal short-circuit.	
Title: NTSB Battery Tests - Final Report For 787 Battery (Asset 436) Tested At 70°C, Ungrounded		
Author(s)	Department	Email
Paul Brazis Pravinray D. Gandhi	Corporate Research	Paul.brazis@ul.com Pravinray.d.gandhi@ul.com
Reviewer(s)	Department	Email
J. Thomas Chapin	Corporate Research	j.thomas.chapin@ul.com



ACKNOWLEDGEMENTS

The authors would like to thank the following individuals for their significant contributions to this work:

Dana Schulze, Bob Swaim, Mike Bauer, Dave Helson, and Mike Hauf from the NTSB.

Simon Lie, Mehdi Barekatein, and Jim Russell from Boeing, Inc.

The authors also would like to thank the following UL employees for their significant contributions to this work:

Paul Courtney
David Dubiel
Alvin Wu
Carl Wang
Laurie Florence
Dan Steppan
Lyle Wright



TABLE OF CONTENTS

Notice	2
Acknowledgements	3
Final Report for 787 Battery (Asset 436) Tested at 70°C, Ungrounded	6
Background	6
Battery Asset 436 Characterization and Preparation	6
Nail Penetration Test	7
UL Test Facility	7
Nail Penetration Battery Test Fixture	8
Instrumentation and Data Acquisition	10
Heat and Smoke Release Measurement System	10
Gas FTIR Analyzer	15
Videos and Photography	15
Battery and Cell Electrical and Thermal Measurement	15
Test Procedures.....	18
Results	19
Test Observations	19
Heat, Smoke, and Vent Effluent Analysis	24
Smoke Release Analysis.....	25
Gas Effluent Analysis	26
Electrical and Thermal Testing Data and Analysis.....	28
Post Test Disassembly	57
Appendix A – Post-Test Disassembly Photos.....	60
Post- Test Photos – Nail Penetration Apparatus and Intact Battery	60
Post Test Disassembly Photos – Top of Battery	61
Intact Battery Post Test Disassembly Photos – Cell Removal.....	62
Battery Post Test Disassembly Photos – Cell 1	69
Battery Post Test Disassembly Photos – Cell 2	71
Battery Post Test Disassembly Photos – Cell 3	73



Battery Post Test Disassembly Photos – Cell 4	75
Battery Post Test Disassembly Photos – Cell 5	77
Battery Post Test Disassembly Photos – Cell 6	79
Battery Post Test Disassembly Photos – Cell 7	82
Battery Post Test Disassembly Photos – Cell 8	85
Appendix B – Battery Pre-Test Disassembly Analysis	87
Internal Battery Disassembly	87
Bus Bar Observation	89
Equipment Documentation	89
OCV Measurement	90
Cell Observations	90
Equipment Documentation	91
Cell Dimension and Weight Measurement	91
Appendix C1 – Infrared Spectra from Asset 436 Nail Penetration Test	96
Appendix C2 – Infrared Spectra from Asset 436 Nail Penetration Test	100



FINAL REPORT FOR 787 BATTERY (ASSET 436) TESTED AT 70°C, UNGROUNDED

Background

NTSB requested UL to conduct nail penetration tests on Boeing 787 batteries under controlled conditions. The batteries tested were of the original ("901") design. NTSB specified that these tests be conducted under a controlled (indoor laboratory) environment and prescribed that the tests be conducted at 100% state-of-charge. There was a desire to investigate the effect of ungrounded versus grounded (through battery charger) batteries to determine the effect on failure behavior. UL provided additional measurements, including heat release, smoke release, and characterization of smoke emissions. Temperature and voltage measurements, as well as wideband frequency measurements were conducted during each test. Batteries were provided by Boeing by the request of NTSB, and witnessed by NTSB investigators, as well as a Boeing engineer. Details regarding the battery sample are provided in the next section.

Battery Asset 436 Characterization and Preparation

The battery test sample (Asset 436) was provided by Boeing at the request of NTSB and shipped to UL Taiwan for disassembly, analysis, and characterization. The following non-destructive tests were performed on battery Asset 436:

- Battery disassembly and measurements (torque, DC/AC resistance and open-circuit voltage (OCV) of cells in the case)
- Cell measurements (visual inspection, weight, dimensions, OCV, AC/DC resistance)
- Computed Tomography (CT)
- Rate capacity measurements (Charge to 100% state-of-charge(SOC) -> Discharge to 0% SOC -> Charge to 100% SOC -> Discharge to 0% SOC -> Charge to 100% SOC by standard procedure under 25°C ambient)
 - Standard charge procedure: CC-CV, 46A to 4.025V for 3 hours
 - Standard discharge procedure: CC at 70A to 2.75V
- Initial discharge profile at -18°C (Discharge to 0% SOC at -18°C)
- EIS under 25°C and -18°C at 0% SOC
- Aging sorting test (0% SOC, stay under 45°C for 3 days)
- Discharge profile at 25°C – Cell 1,3,4,6
 - Charge to 100% SOC -> Discharge to 0% SOC -> Charge to 100 SOC
- Discharge profile at -18°C – Cell 1,3,4,6



- Charge to 100% SOC -> Discharge to 0% SOC - >Charge to 100 SOC
- Discharge all cells to 3.75V for shipping
- Attach thermocouples and strain gages
- Reassemble battery

Details of the battery disassembly and pre-test characterization can be found in Appendix B of this report.

Nail Penetration Test

The nail penetration test was performed at UL's Northbrook facilities. The battery was equipped with additional test measurement leads as described later in the report.

UL Test Facility

The tests were conducted in UL's Cell A test facility. The test cell is a 35 x 35 x 40 ft. high test room equipped with a 14 x 14 ft. collection hood to collect fire effluents (smoke, and gases). The collection hood is connected to UL's smoke abatement system through a 24 in. exhaust duct. Incorporated in the exhaust duct, is an instrumented section for measurement of smoke density and gases from a fire. The smoke density is measured using a photometric system consisting of a white light source and a photo detector to measure the opacity of the smoke. Heat release rate is calculated using an oxygen consumption technique¹. To enable this, duct velocity is monitored using a bi-directional probe, and the exhaust gases are monitored using a paramagnetic oxygen analyzer. The heat release rate system in Cell A has a capacity to measure a maximum 2 MW fire size.

A photograph of the Cell A is shown in Figure 1.

¹ W. J. Parker, "Calculations of Heat Release Rate by Oxygen Consumption for Various Applications", U. S. Department of Commerce, National Bureau of Standards, Center for Fire Research, Washington DC, 20234, NBSIR 81-2427-1, (1982).



Figure 1. Cell A

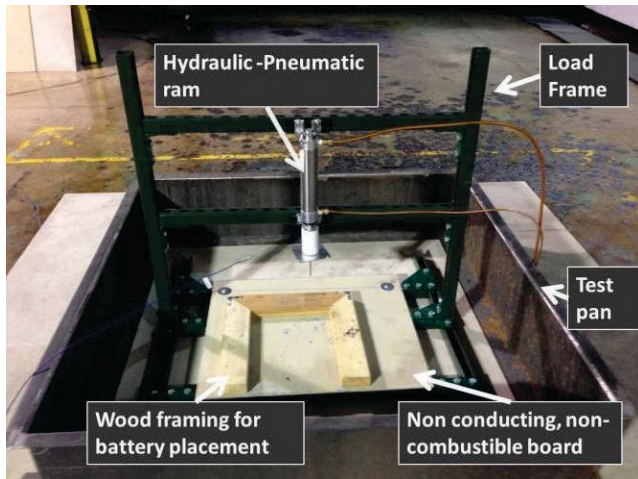
Nail Penetration Battery Test Fixture

A nail penetration test fixture was developed to enable controlled nail penetration of the test batteries. The set-up included a load frame with a fixture that contained a nail penetration ram. The ram was designed such that its downward direction was controlled using hydraulic fluid pressurized by compressed air; and upward direction was controlled by compressed air. A photograph of the nail penetration test set-up is shown in Figure 2.

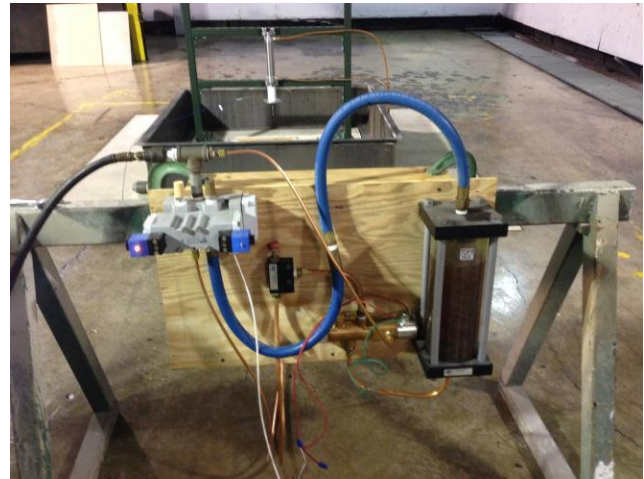
A non-conducting and non-combustible board was placed at the bottom of the load frame, and a wood frame screwed into the board to allow precision placement of the test battery with respect to the nail.

A specially designed nail² was used in the test. The nail is 126 mm long, with a diameter of 5 mm, and nail angle of 60°. A unique feature of the nail is an embedded thermocouple that provides temperature of the cell as it penetrates the battery. An annotated photograph of the nail is presented in Figure 3.

² Type B, Number 1 nail from Yamamoto Technologies Company Limited, 4-7, Setoguchi 2-Chome, Hirano-Ku, Osaka 547-0034 Japan.



Test Fixture



Hydraulic-Pneumatic Control System

Figure 2. Nail Penetration Test Set-Up

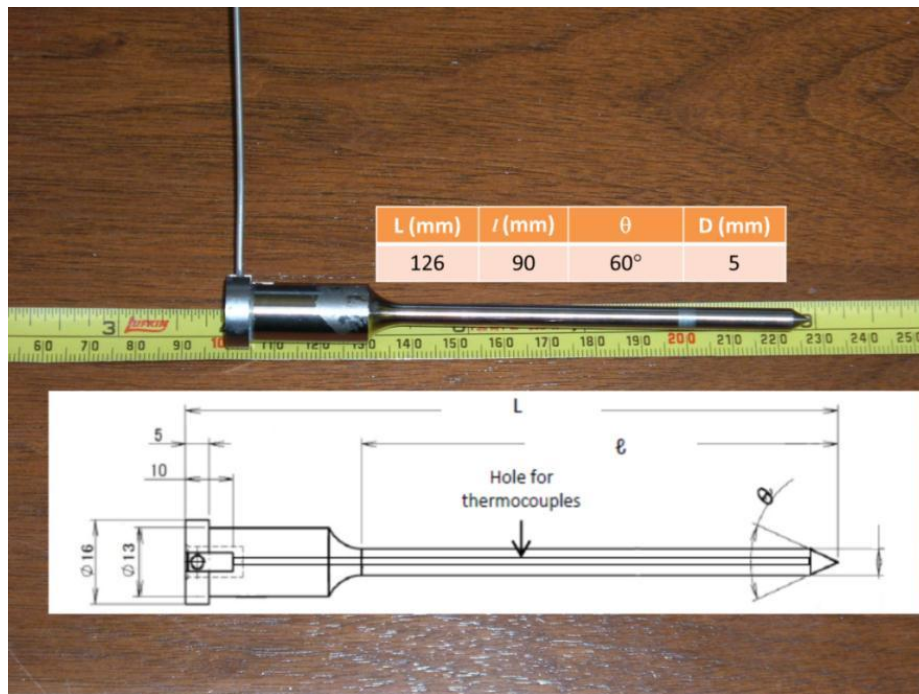


Figure 3. Test Nail

A close-up of the nail in the load frame is shown in Figure 4.



Figure 4. Test Nail in Load-frame

Instrumentation and Data Acquisition

Heat and Smoke Release Measurement System

The heat release rate is calculated using oxygen consumption technique. The system consists of a paramagnetic oxygen analyzer to measure the oxygen concentration; and bi-directional probe and thermocouple to measure the exhaust duct velocity. The smoke release rate is calculated using light transmission measurement consisting of a regulated light source, and a photoelectric detector. The measurement equipment used is described herein.

Oxygen Concentration Measurement

The oxygen analyzer was Siemens Oxymat 6 with a range from 0 to 25% oxygen.

Velocity Measurement

The velocity is measured using a bi-directional probe and a thermocouple. A schematic of the bi-directional probe is shown in Figure 5.

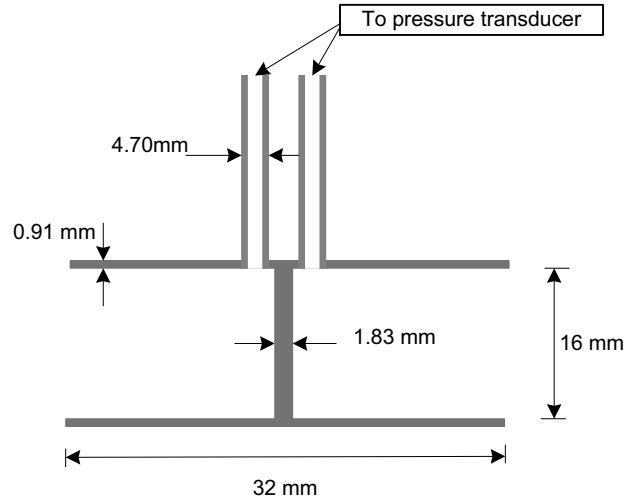


Figure 5. Bi-directional Probe

The bi-directional probe was connected a pressure transducer (MKS, Model: 220B) with a range of 0 – 10 mm Hg. The thermocouple used was 0.125 mm Inconel sheathed, Type K thermocouple.

The pressure and velocity data was used to calculate the flow velocity using Eq. 1.

$$V = C_v \sqrt{\Delta P \cdot T} \quad \text{Eq. 1}$$

where

- V is the velocity (m/s);
- C_v is the calibration constant for the bi-directional probe (= 0.806)
- ΔP is the pressure difference across the bi-directional probe (mm Hg); and
- T is flow temperature (K);

Smoke Density Measurement

The smoke optical density was measured using a white light source and a Photronic cell (Weston, Model: 856-9901013-BB). The optical density is calculated as a function of transmitted light using Eq. 2.

$$OD = \text{Log}_{10} \left(\frac{I_o}{I} \right) \quad \text{Eq. 2}$$

where

- OD is the optical density;

- I_o is the clear beam signal (V); and
- I is the test signal (V).

Calibration of Heat and Smoke Release Rate Measurements

The heat release rate system was calibrated using propane gas sand burner with known fire sizes of 75, and 200 kW; and a calibration factor was calculated. This range of the calibration fire sizes were selected based upon anticipated fire size during the test. The calibration for heat release rate is depicted in Figure 7. A calibration factor of 0.92 was applied to the calculation of heat release rate data during the test.

A photograph of the set-up used for heat release rate calibration is presented in Figure 6.



Figure 6 – Heat Release Rate Calibration Set-Up

The heat release rate is calculated using exhaust flow, and oxygen concentration data as shown in Eq. 3.

$$HRR = C_1 \cdot 17.15 \times 10^3 \cdot A \cdot V \cdot \left(\frac{298}{T} \right) \left(\frac{0.2095 - O_2}{\alpha - \beta O_2} \right) \quad \text{Eq. 3}$$

where

- C_1 is calibration factor (equal to 0.92)
- 17.15×10^3 is energy release per volume of oxygen consumed at 298 K (kJ/m³)
- A is duct area (m², equals 0.2919 for Cell A system)
- V is exhaust flow velocity (m/s)
- T is exhaust flow temperature (K)
- O_2 is oxygen concentration
- α constant for propane gas (equals 1.084)
- β constant for propane gas (equals 1.4)

The smoke measurement system was calibrated using neutral density filters. The calibration for the smoke measurement system is shown in Figure 8. A correction factor of 0.98 was applied to the calculated optical density data from the test.

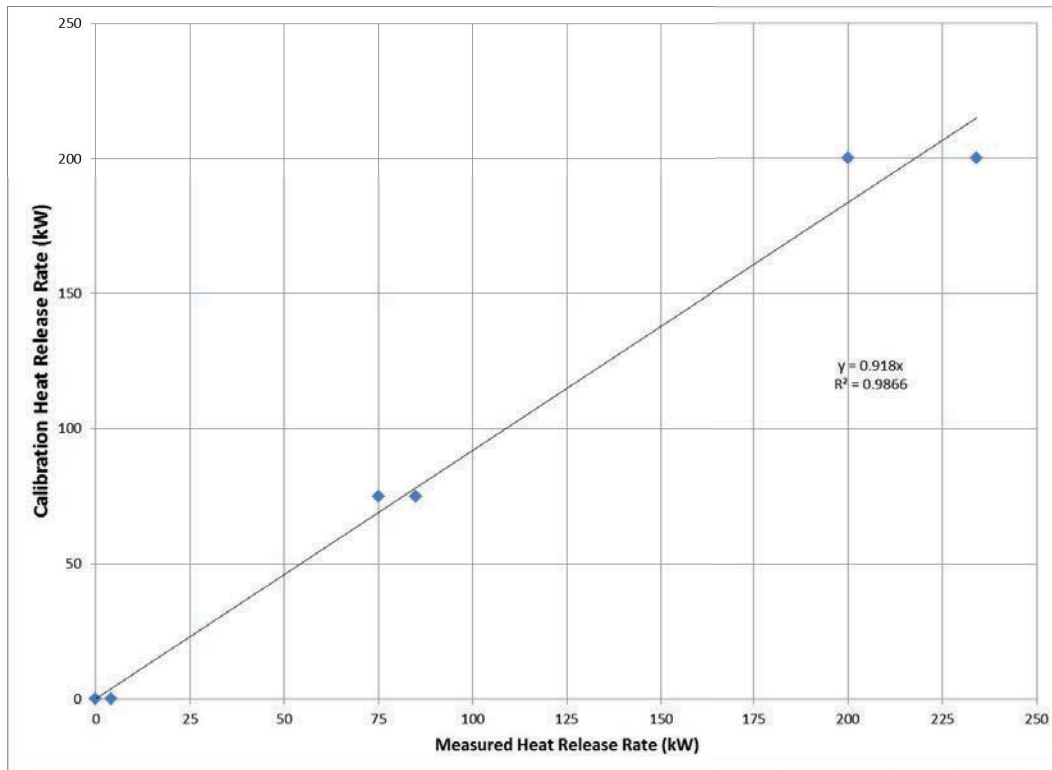


Figure 7. Heat release rate calibration

The smoke measurement system was calibrated using reference neutral density filters and the transmitted light output was used to calculate optical density as shown in Eq. 4.

$$OD = \text{Log}_{10} \left(\frac{I_o}{I} \right) \quad \text{Eq. 4}$$

where

- OD is the calculated optical density
- I_o is the clear beam signal (volts)
- I is the transmitted light signal (volts)

A calibration constant was then developed by correlating the calculated optical density with the neutral density filters as shown in Figure 8.

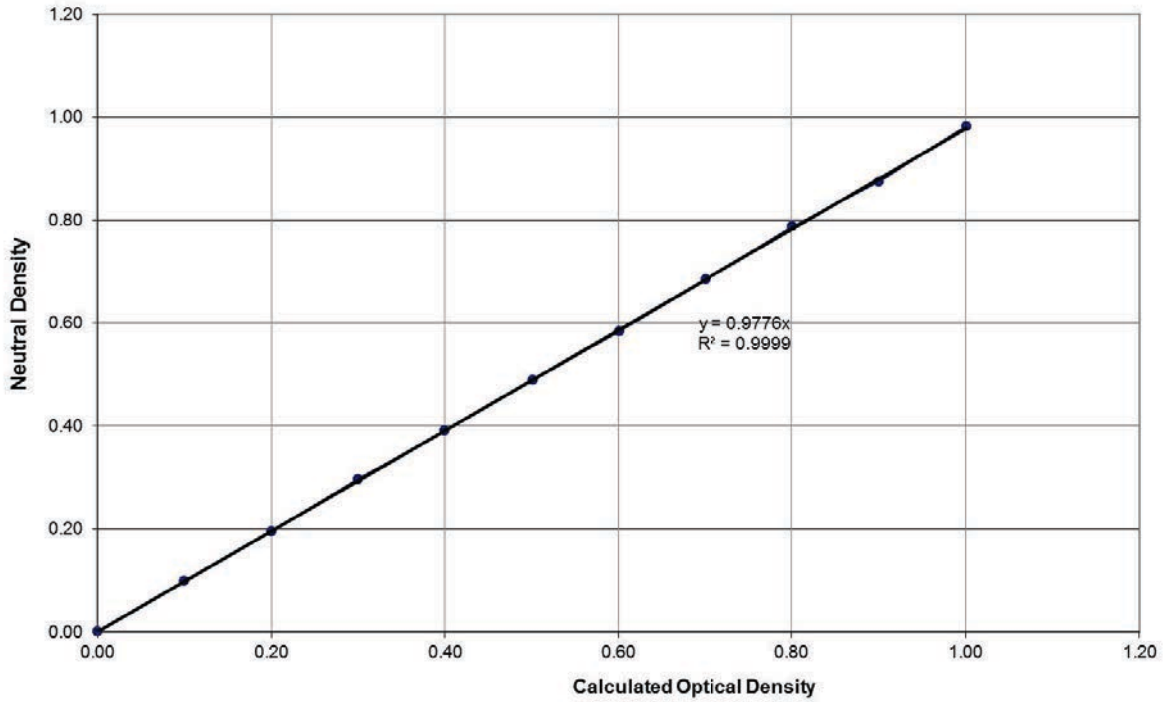


Figure 8. Smoke obscuration system calibration.

Smoke release rate is calculated using optical density and duct velocity data as shown in Eq. 5.

$$SRR = C_2 \frac{V \cdot A}{L} \text{Log}_{10} \left(\frac{I_o}{I} \right) \quad \text{Eq. 5}$$



where:

- C_2 is the optical density calibration factor (=0.98)
- SRR is smoke release rate (m^2/s)
- V is exhaust flow velocity (m/s)
- A is duct area (m^2 , equals 0.2919 for Cell A system)
- L is the path length (m , equals 0.6096 m for Cell A system)
- I_o is the clear beam signal (volts)
- I is the signal during the test (volts)

Gas FTIR Analyzer

A heated gas sampling probe, connected to a gas FTIR analyzer, was added to the instrumented duct section to extract the gases vented from the test battery during the test. The gas FTIR analyzer has a resolution of 0.5 cm^{-1} , and a path length of 10 m and can measure gas signatures in the range from $650 - 4500\text{ cm}^{-1}$. The FTIR analyzer continuously extracted gases from the instrumented duct at a rate of 4.2 L/min. The analyzer developed an average of 4 scans and provided an overall gas sampling rate of approximately 10 samples per minutes.

Videos and Photography

Digital video and still photography was used to document the tests. A total of five video cameras, and two Infra-red cameras were used to capture the fire tests from different angles. Three digital still photography cameras were used to capture key events during the tests.

Battery and Cell Electrical and Thermal Measurement

Figure 9 shows a photograph of the voltage and temperature cabling installed within the battery. Two types of thermocouples were utilized for temperature measurements for the tests. Type J thermocouples had been previously attached to the battery, used for non-destructive testing. These thermocouples consisted of 40 AWG insulated cabling, with insulation that is not intended for high-temperature applications. These thermocouples were attached using cyanoacrylate compounds, with the thermocouple junctions embedded within this cyanoacrylate material so that the junction was not in electrical contact with the battery components. External to the battery, these thermocouples were attached to a DIN rail interface (Figure 10), which connected the Type J thermocouples to thermocouple extension cabling that extended the cabling to the instrumentation.

The remaining thermocouples used for temperature measurement were Omega Nextel® Ceramic-Braided Type K thermocouples, XC Series. These thermocouples were 24 AWG and shielded with a ceramic-braided material for increased thermal resistance, rated for continuous use at 1200°C. Sixteen of these Type K thermocouples were added to the top surface (Face 5) of each battery cell, located on the busbars nearest each cell terminal. To optimize the thermal interconnection, the junction was attached directly under voltage sensing screws that are included as a part of the battery construction. For both thermocouple types, locations for each thermocouple are detailed for each cell discussion in the data analysis section.

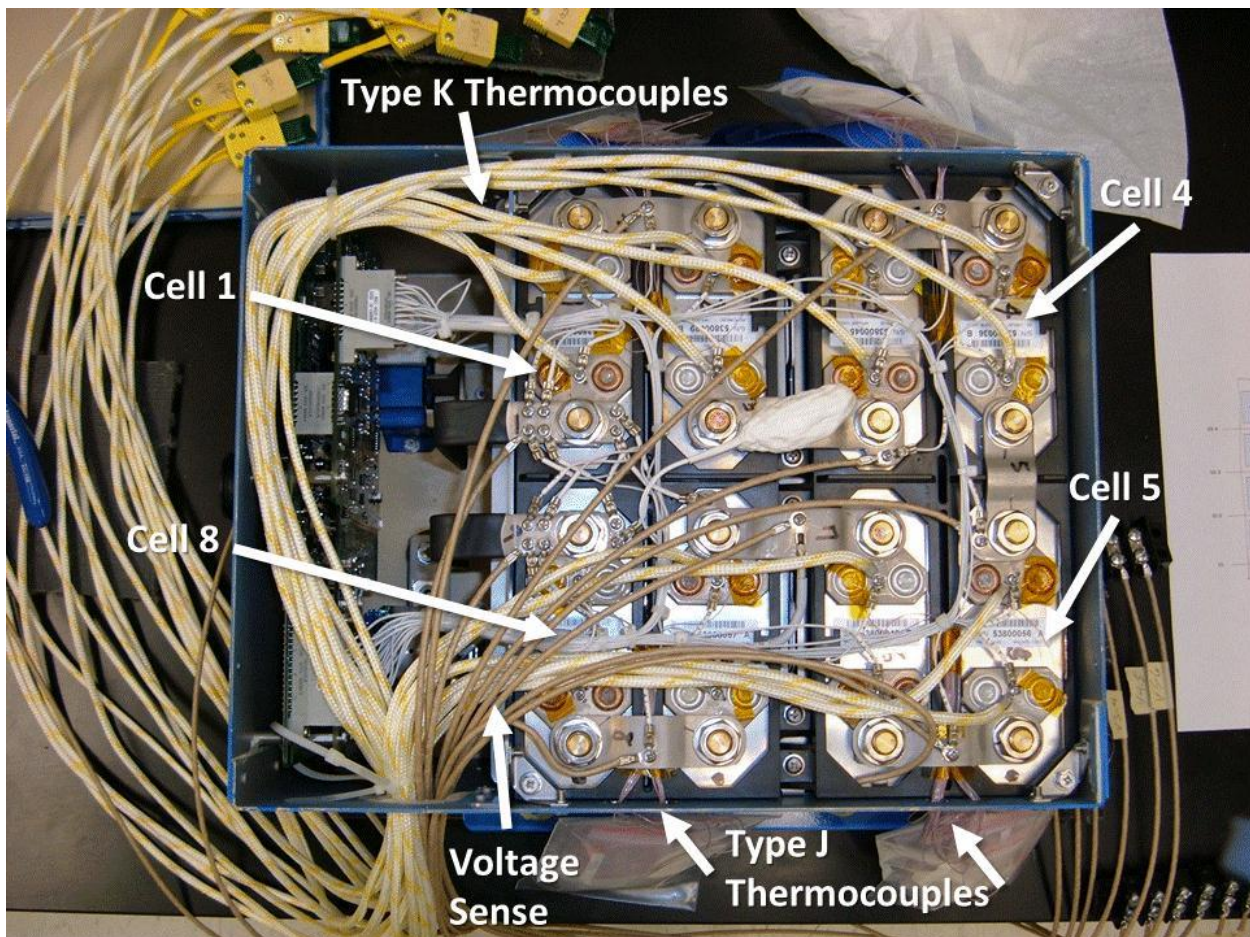


Figure 9. Photo of voltage and temperature sensing wiring for 70°C battery. Image taken before installation of coaxial cabling.

Voltage leads were attached at nine electrical nodes in order to monitor the voltage across each of the eight cells. Three additional voltage leads were added to monitor the voltage at the grounding connector on the battery box, the voltage on the case of Cell 6, and the voltage at the positive terminal on the main



battery power connector. Ground and battery voltages were referenced to the negative terminal of the battery (connected to the negative terminal of Cell 1). These voltage leads were constructed using insulated oven wire, Type MG, nickel-plated copper, shielded with fiberglass insulation over mica tape. This cable is specified for operation at 840°F, selected to maximize operational lifetime for the test.

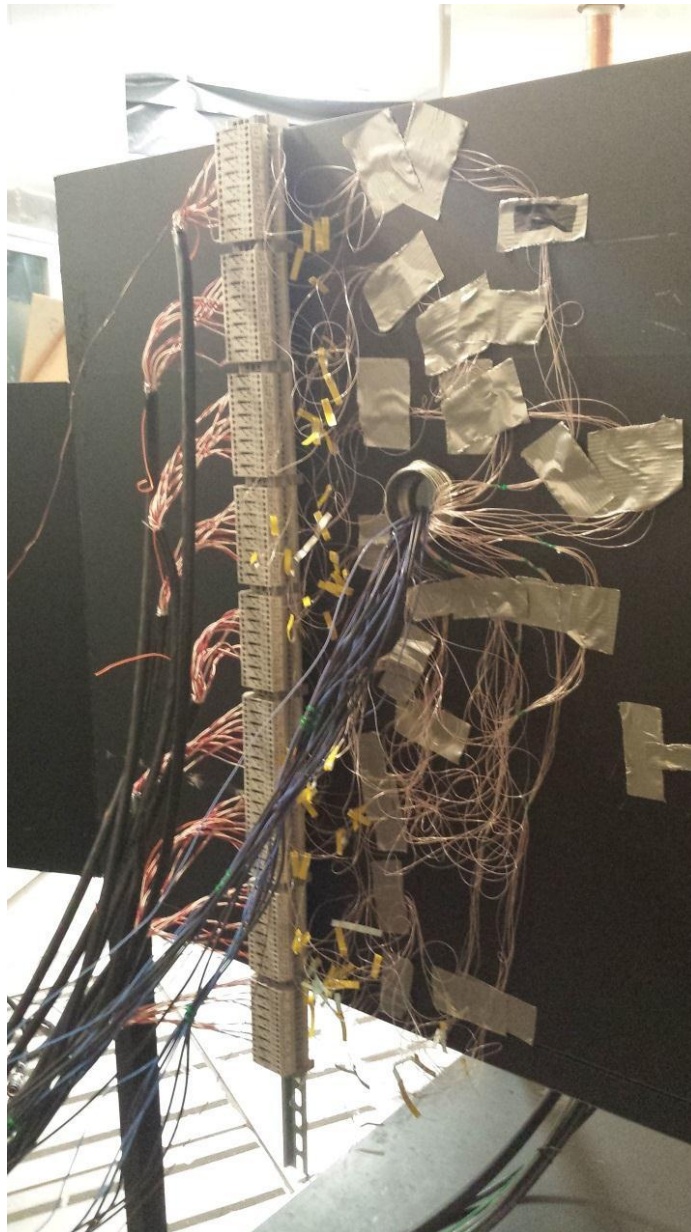


Figure 10. DIN rail interface for Type J thermocouples, shown used during prior non-destructive battery testing.



Voltage leads were made by crimping ring terminals to each of the voltage leads, and then attached using the existing screw terminals. The case connection to Cell 6 was made through compression of a bare voltage sense lead between the metal case of Cell 6 and the black plastic frame holding Cell 6 into the battery assembly. This interconnect was verified using a handheld multimeter and mechanically checked for integrity after installation.

The voltage and temperature leads were connected to two Agilent Model 34970A Data Acquisition Switch Units, which enabled scanning and recording of the data. Thermocouple and voltage leads were interfaced to these units using six Agilent Model 34901A relay cards. These units were then connected via GPIB interface to a laptop computer for data acquisition. Data for all voltage, current, and temperature channels were recorded in CSV format, approximately every 2-3 seconds.

Coaxial cables were attached to each of the two terminals of Cell 6 in order to measure spectral noise. These coaxial cables were stripped of their outer insulation and shield to a distance of 18 inches from the cable end to minimize potential shorting of the coaxial ground to live parts in the battery during test. Interconnects were made using a crimped ring terminal that was then attached to existing screw terminals across Cell 6. The coaxial cable was thermally shielded using ¼ inch glass braid from the interconnect point out to a minimum of 12 inches after exiting the battery case. The coaxial cable was then connected to a high-speed digitizer card (National Instruments Model PXI-5922) via a differential probe. The differential signal across Cell 6 was recorded repeatedly, each for duration of 100 ms. Due to instrument limitations, continuous recording was not attainable. Over the course of the entire test, 740 samples of 100 ms each were recorded. These were then processed using LabVIEW-based automated software to calculate FFT spectra and record maximum, minimum, and average magnitude at each frequency point over the 740 spectral files.

Test Procedures

For both the batteries, the following test procedures were used.

1. Remove the battery from the conditioning chamber.
2. Connect the battery sensors (e.g., voltage, thermocouples) to data acquisition system.
3. Place the battery in the nail penetration test fixture and connect all sensors to the data acquisition system.
4. Conduct safety review.
5. Verify all instrumentation, video and photographic documentation are working.
6. Document the individual cell voltages.
7. Start 1 minute countdown.

8. Initiate test by energizing the piston to penetrate the battery at a rate of 1 mm/s; continue nail penetration when open circuit voltage (OCV) dropped.
9. Continue data collection until directed by NTSB staff to stop.

Results

Test Observations

During the test, photographs were taken to document the venting of the battery after nail penetration. These are presented in the series on photographs below.

Test Photos – reference NPT initiation 2:39

Battery photo (approximately 54 seconds after initiation of nail penetration)

Ref G0010349 photo 2:40



Battery photo (approximately 54 seconds after initiation of nail penetration)

Ref G0010350 photo 2:40



Battery photo (approximately 6 minutes after initiation of nail penetration)

Ref G0010359 photo 2:45



Battery photo (approximately 7 minutes after initiation of nail penetration) – Ref G0010360 photo 2:45



**Battery photo (approximately 10 minutes after initiation of nail penetration)
Ref G0010367 photo 2:49**



Battery photo (approximately 11 minutes after initiation of nail penetration)

Ref G0010368 photo 2:49



Battery photo (approximately 16 minutes after initiation of nail penetration)

Ref G0010380 photo 2:55



Battery photo (approximately 19 minutes after initiation of nail penetration)

Ref G0010385 photo 2:58



Battery photo (approximately 20 minutes after initiation of nail penetration)

Ref G0010387 photo 2:59



Battery photo (approximately 20 minutes after initiation of nail penetration)

Ref G0010388 photo 2:59



Heat, Smoke, and Vent Effluent Analysis

Heat release, smoke release, and gases were analyzed from the venting battery. *While the battery vented, there were no observations of flaming external to the battery.*

The heat release rate is calculated using exhaust flow, and oxygen concentration data as shown in Eq. 6.

$$HRR = C_1 \cdot 17.15 \times 10^3 \cdot A \cdot V \cdot \left(\frac{298}{T} \right) \left(\frac{0.2095 - O_2}{\alpha - \beta O_2} \right) \quad \text{Eq. 6}$$

where

- C_1 is calibration factor (equal to 0.92)
- 17.15×10^3 is energy release per volume of oxygen consumed at 298 K (kJ/m³)
- A is duct area (m², equals 0.2919 for Cell A system)
- V is exhaust flow velocity (m/s)
- T is exhaust flow temperature (K)
- O_2 is oxygen concentration
- α constant for testing with complex chemistries (equals 1.105)
- β constant for testing with complex chemistries (equals 1.5)

The heat release rate data for the test is shown in Figure 11. While no external flaming was observed, the relatively small values heat release rate may be indication of oxidation of the vent gases in air.

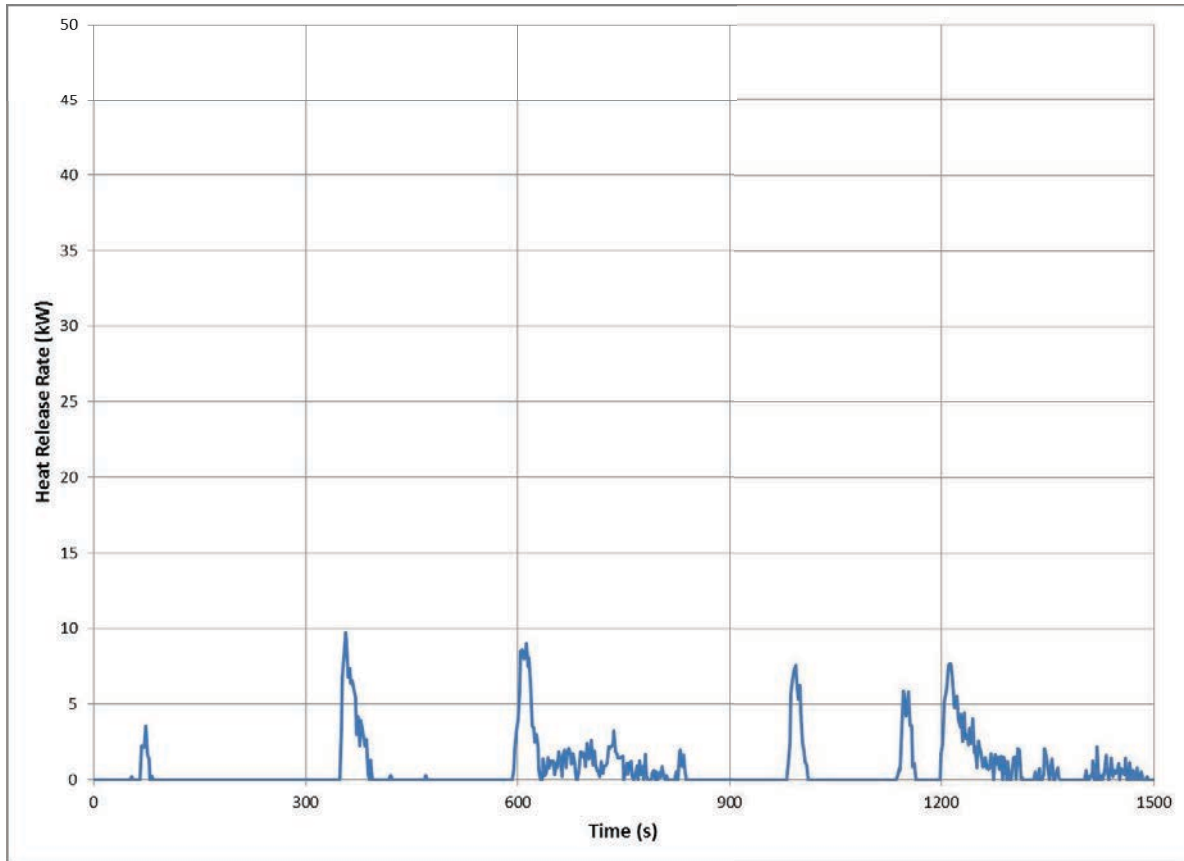


Figure 11. Heat Release Rate data from the 70°C test

Smoke Release Analysis

Smoke release rate is calculated using optical density and duct velocity data as shown in Eq. 5. The smoke release rate data are presented in Figure 12. The data shows distinct release of gases after the Cell 6 was shorted with nail penetration procedure, can be correlated with cell temperature and voltage data obtained during the test.

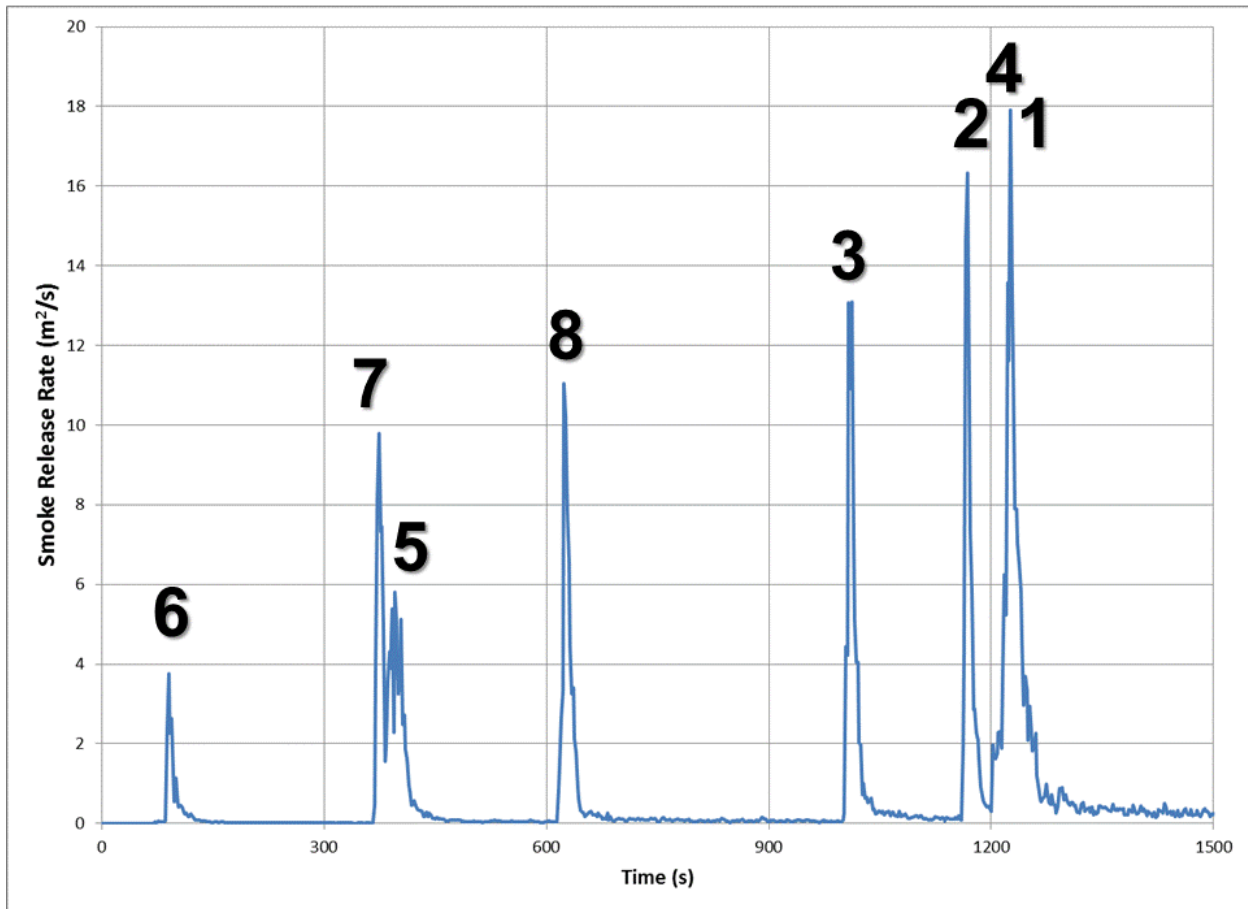


Figure 12. Smoke release rate data from the 70°C test. Numbers in graph denote cell which is venting at the moment of each peak (see Figure 38 for corresponding electrical data).

Gas Effluent Analysis

Gas effluent analysis is a specific method to define gas species by using FTIR technique. Aldrich vapor phase sample library, EPA vapor library, and UL in house library were used to identify the species in the effluent. The vent events were tagged as shown in Figure 13 to enable identification of gases related to each vent event.

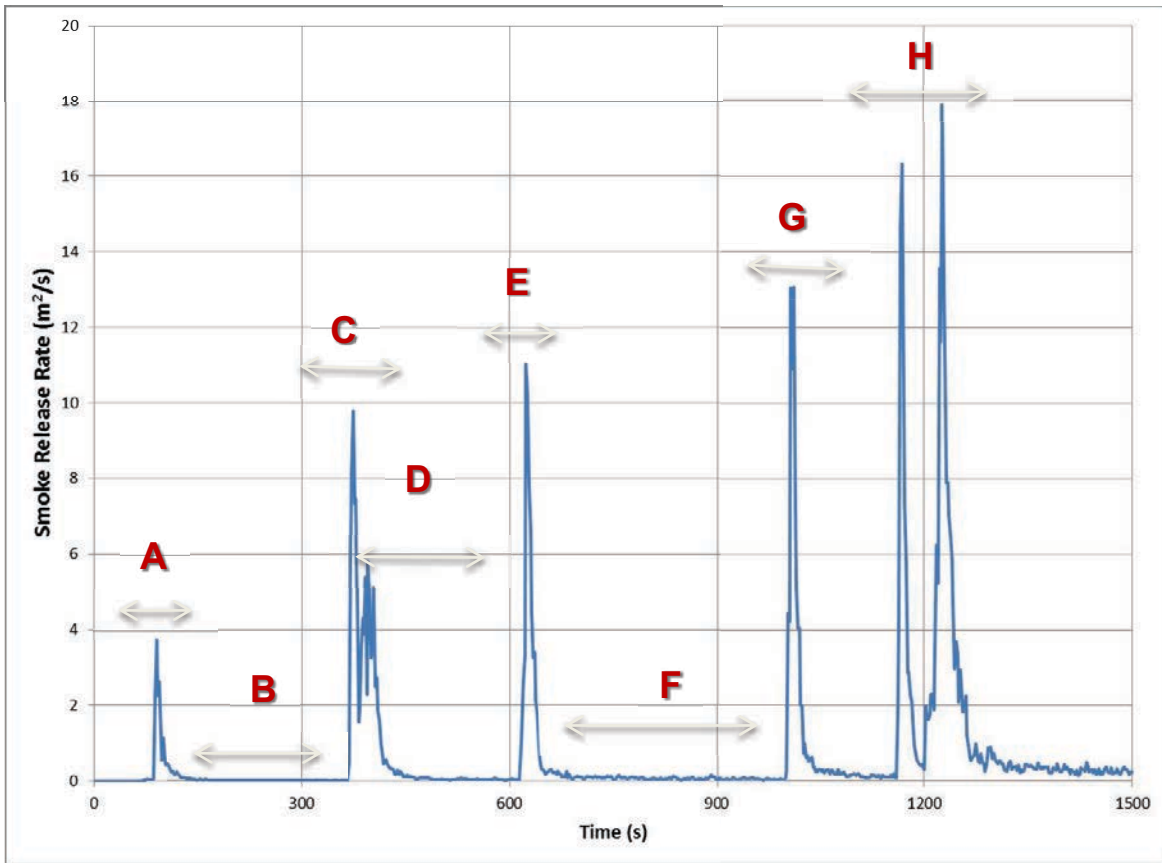


Figure 13 –Vent Events Identified for Gas Analysis

The gas effluent analysis for each of the vent events is presented in Table 1. In each venting period (Zone A, C, E, G and H), the species in the vented smoke include the solvents in electrolyte, small hydrocarbons, CO, CO₂ and water. In the later venting period (Zone D, E, G and H), the vented smoke additionally contains the species which are suspected to be generated from oxidation/pyrolysis of the packaging materials surrounding the cells.



Table 1 – Gas Analysis for Vent Events

Zone	Gas Species	Time Duration *	Peak High *	Remark
A	DMC, EMC, CO ₂ , H ₂ O, CH ₄ , CO, C ₂ H ₄ , C ₂ H ₂	14:30:30' ~ 14:34:29'	14:31:16' ~ 14:32:03'	Please see Appendix C1 for IR spectra
B	DMC, CO ₂ , H ₂ O, CH ₄	14:34:36' ~ 14:35:43'		
C	DMC, EMC, CO ₂ , H ₂ O, CH ₄ , CO, C ₂ H ₄ , C ₂ H ₂	14:35:49' ~ 14:38:16'	14:35:55' ~ 14:36:56'	
D	DMC, EMC, CO ₂ , H ₂ O, CH ₄ , CO, C ₂ H ₄ , C ₂ H ₂ , EC, CH₃OH, HCl, C₆H₆	14:37:36' ~ 14:39:49'		Please see Appendix C2 for IR spectra
E	DMC, EMC, CO ₂ , H ₂ O, CH ₄ , CO, C ₂ H ₄ , C ₂ H ₂ , EC, CH₃OH, HCl, C₆H₆	14:39:56' ~ 14:42:09'	14:40:03' ~ 14:40:56'	
F	DMC, CO ₂ , H ₂ O, CH ₄ , CO, C ₂ H ₄ , C ₂ H ₂ , EC, CH₃OH, HCl, C₆H₆	14:42:16' ~ 14:46:16'		
G	DMC, EMC, CO ₂ , H ₂ O, CH ₄ , CO, C ₂ H ₄ , C ₂ H ₂ , EC, CH₃OH, HCl, C₆H₆	14:46:23' ~ 14:48:36'	14:46:29' ~ 14:47:23'	
H	DMC, EMC, CO ₂ , H ₂ O, CH ₄ , CO, C ₂ H ₄ , C ₂ H ₂ , EC, CH₃OH, HCl, C₆H₆	14:48:43' ~ 14:57:10'	14:49:10' ~ 14:51:16'	

DMC = Dimethyl carbonate; EMC =Elthymethyl carbonate; EC = Ethylene carbonate; CO = Carbon monoxide.

Electrical and Thermal Testing Data and Analysis

The following sections describe the failure of each cell during the 70°C test, described in order of venting of each cell. During the venting event, each exhibits an initial drop in voltage, likely due to the internal shorting of one of the three sub-cells within each cell. Since this first internal short signifies the beginning of cell failure, electrical and thermal data in this report are given at the moment of this initial voltage drop. Data are also given at the moment the entire cell fails completely, at the moment the drop to zero volts begins. These correspond to the failure of the first of three internal cells and the failure and subsequent venting of the cell. The following sections describe in detail the time of failure for each of the eight cells, showing thermocouple temperatures for each of the two instances when voltage drops, each cell listed in chronological order. Values in parentheses denote values that result from thermocouples that exhibited increased noise or failed soon afterwards and therefore may not show as reliable data as that for thermocouples that remained fully intact throughout the test.



Initial Cell Voltages

The battery was fully charged prior to temperature conditioning and testing. Table 2 shows the voltages of each cell prior to start of the nail penetration test.

Table 2. Cell voltages at start of test.

Cell	1	2	3	4	5	6	7	8
Voltage (V)	4.02838	4.01602	4.02721	4.02161	4.00924	4.02057	4.01669	4.01496

Failure Timeline

Shows the failure times for each of the eight cells. The following sections describe electrical and thermal behavior for each cell in more detail, in the order of cell venting sequence.

Table 3. Timeline for venting of each of the eight cells, test time (in seconds) shown.

	Cell Number							
	6	7	5	8	3	2	4	1
Onset of Initial Voltage Drop	60	357	360	603	993	1152	996, 1185	1209
Onset of Voltage Drop to Zero	75	363	381	612	999	1158	1200	1215
Immediately After Drop to Zero	84	369	396	621	1002	1161	1209	1221

Table 4. Timeline for venting of each of the eight cells, time (mm:ss) relative to nail penetration of Cell 6 shown.

	Cell Number							
	6	7	5	8	3	2	4	1
Onset of Initial Voltage Drop	0:00	4:57	5:00	9:03	15:33	18:12	15:36, 18:45	19:09
Onset of Voltage Drop to Zero	0:15	5:03	5:21	9:12	15:39	18:18	19:00	19:15
Immediately After Drop to Zero	0:24	5:09	5:36	9:21	15:42	18:21	19:09	19:21

Cell 6

Failure of Cell 6 was initiated by nail penetration through Face 5, triggering an internal short circuit and subsequent failure of the cell. The voltage curve suggests that at this moment one of the three sub-cells failed and formed an internal short-circuit. This caused the initiation of significant internal heating, observed on the nail, as well as locations on Faces 4, 3, 2, and 1 (in rough order of magnitude). Three seconds after nail penetration this sub-cell opens and the voltage on Cell 6 recovers. Face temperatures continue to rise, but the rate slows, likely due to removal of the internal short circuit path. Fifteen seconds after nail penetration the cell begins to vent, showing a drop to zero voltage and rapid rise of temperatures throughout the cell. As can be seen in Figure 16, the nail temperature shows the highest temperature (peaking at 535.3°C at 132 seconds into the test, or 1:12 after nail penetration). Temperatures at Faces 1-4 range between 200°C to 400°C one minute past nail penetration, with the highest temperatures observed at the center line of the cell (thermocouples 6412 and 6212). Heat transfer down each of the two busbars commences once venting occurs, though temperatures at the busbars remains lower than that at the faces of Cell 6.

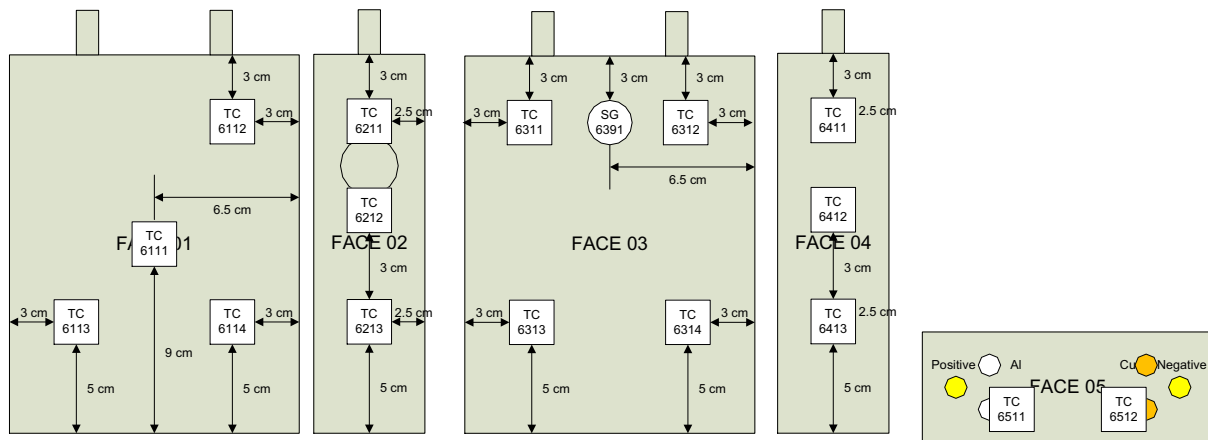


Figure 14. Location of thermocouples attached to Cell 6.



Table 5. Time and temperature data at time of Cell 6 failure.

	Onset of Initial Voltage Drop	Onset of Voltage Drop to Zero	Immediately After Drop to Zero	Maximum Temp.	Time of Maximum Temp. (s)
Test Time (s)	60	75	84		
Time After Nail Penetration (m:s)	0:00	0:15	0:24		
Type K TC Nail (°C)	35.20	452.5	486.6	567.4	432
Type J TC #6111 (°C)	67.58	106.3	139.1	(580)	894
Type J TC #6112 (°C)	-	-	-	-	-
Type J TC #6113 (°C)	67.49	113.4	183.0	(650)	585
Type J TC #6114 (°C)	66.61	143.9	242.7	(550)	609
Type J TC #6211 (°C)	-	-	-	-	-
Type J TC #6212 (°C)	59.27	187.5	286.9	(460)	435
Type J TC #6213 (°C)	58.29	171.9	209.6	(440)	267
Type J TC #6311 (°C)	67.19	177.8	236.0	(450)	417
Type J TC #6312 (°C)	68.58	131.0	172.1	(600)	1053
Type J TC #6313 (°C)	67.83	126.6	163.1	(580)	1212
Type J TC #6314 (°C)	67.83	89.39	143.9	(580)	606
Type J TC #6411 (°C)	-	-	-	-	-
Type J TC #6412 (°C)	68.66	250.6	329.8	(650)	489
Type J TC #6413 (°C)	67.56	247.5	220.6	(680)	999
Type J TC #6511 (°C)*	67.25	118.8	181.3	491.7	1632
Type K TC #6501K (°C)*	66.72	110.4	146.2	492.0	1650
Type J TC #6512 (°C)*	65.34	107.9	159.1	498.9	1053
Type K TC #6502K (°C)*	64.89	108.4	165.5	497.3	1053

*Note: Position 6511 is in same position as 6501K; position 6512 is in same position as 6502K.

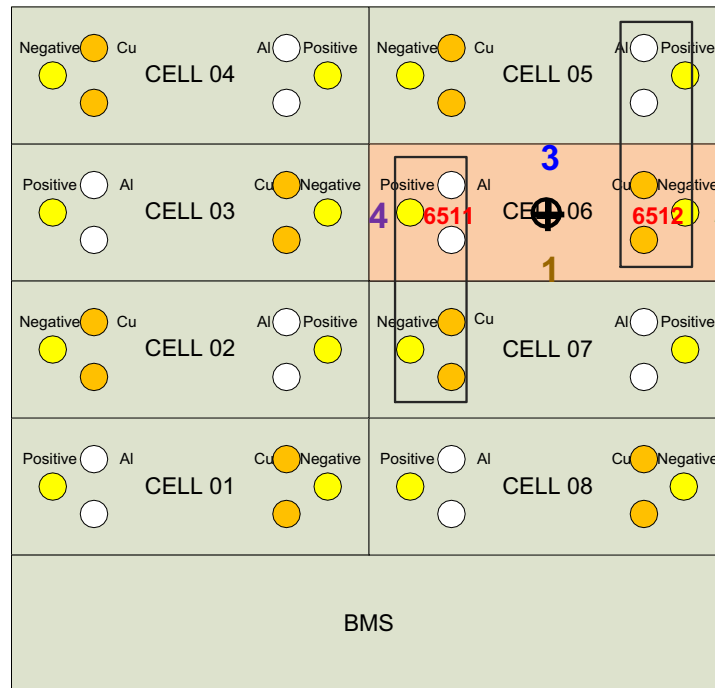


Figure 15. Schematic of the eight cells within the battery, showing location of busbars and designation of each face for Cell 6.

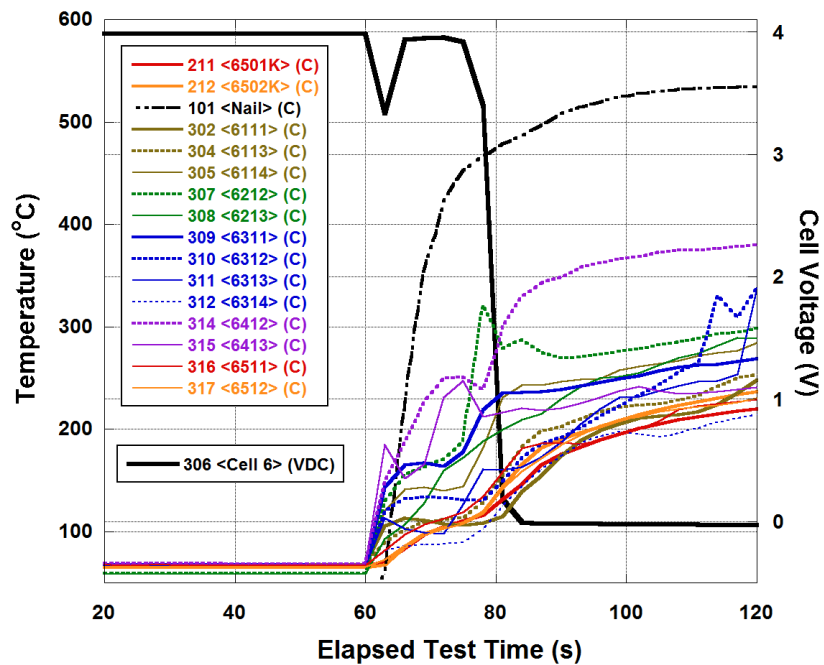


Figure 16. Voltage and temperature data for Cell 6 in the vicinity of the venting event.

Cell 7

Cell 7 was the second cell to vent, and the first cell to vent after the initial nail penetration event. Failure was due to the transfer of thermal energy from Cell 6 to the negative terminal of Cell 7 through the busbar connected between Cells 6 and 7. This is supported by the rising temperature on thermocouple 7502. Though Face 3 was adjacent to the vented Cell 6, no significant temperature rise was observed; however, the adjacent Face 1 of Cell 6 was measured to have the lowest temperatures of the four faces after venting. Immediately following venting of Cell 6, Faces 2 and 4 of Cell 7 exhibit the most heating, possibly due to thermal transfer from vented gases on Face 2 that is adjacent to the vent hole on Cell 6, Face 2. Face 4 may be receiving conducted heat from Face 4 of Cell 6, which was measured to be at the highest temperature of all Cell 6 faces after venting. After venting of Cell 7, Type J thermocouples begin to lose signal quality, and therefore junction/cable integrity, as the temperature rises above 250°C.

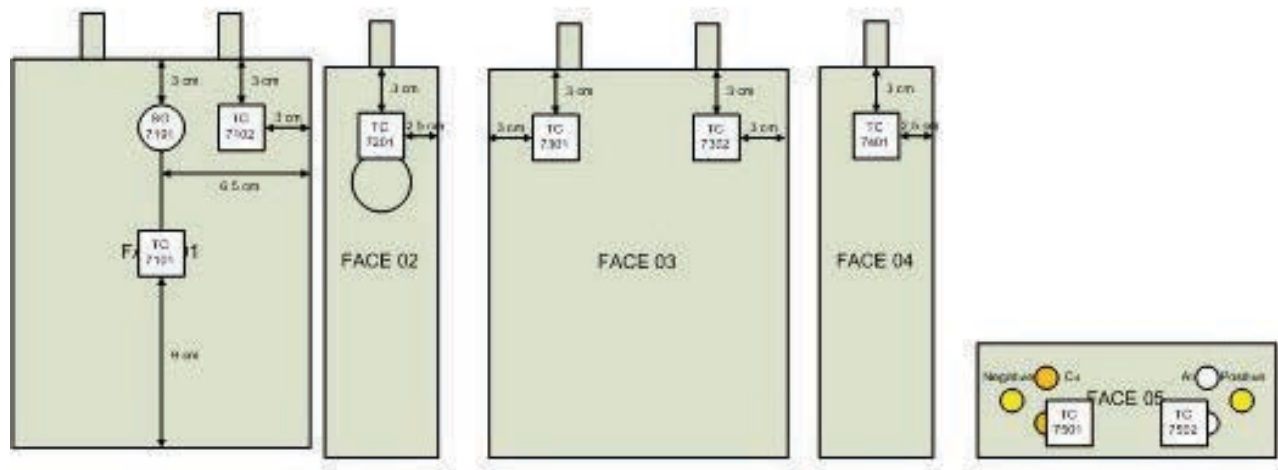


Figure 17. Location of thermocouples attached to Cell 7.



Final Report for 787 Battery (Asset 436) Tested at 70°C, Ungrounded

Table 6. Time and temperature data at time of Cell 7 failure.

	Onset of Initial Voltage Drop	Onset of Voltage Drop to Zero	Immediately After Drop to Zero	Maximum Temp.	Time of Maximum Temp. (s)
Test Time (s)	357	363	369		
Time After Nail Penetration	4:57	5:03	5:09		
Type J TC #7101 (°C)	-	-	-	-	-
Type J TC #7102 (°C)	80.59	85.73	86.4	599.7	1410
Type J TC #7201 (°C)	120.7	184.2	213.8	(580)	897
Type J TC #7301 (°C)	-	-	-	-	-
Type J TC #7302 (°C)	81.70	111.2	147.0	(550)	861
Type J TC #7401 (°C)	112.6	195.4	219.8	(780)	1053
Type J TC #7501 (°C)	163.5	181.7	214.9	511.5	1599
Type K TC #7501K (°C)	163.3	177.2	215.1	531.7	1677
Type J TC #7502 (°C)	97.25	112.9	143.3	-	-
Type K TC #7502K (°C)	96.58	121.0	157.9	516.3	858

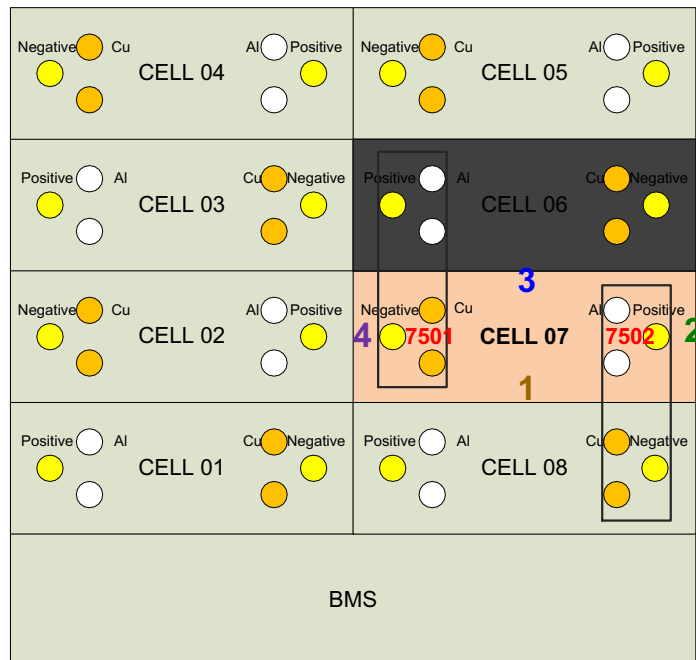


Figure 18. Schematic of the eight cells within the battery, showing location of busbars and designation of each face for Cell 7. Gray shading denotes cells that have previously vented.

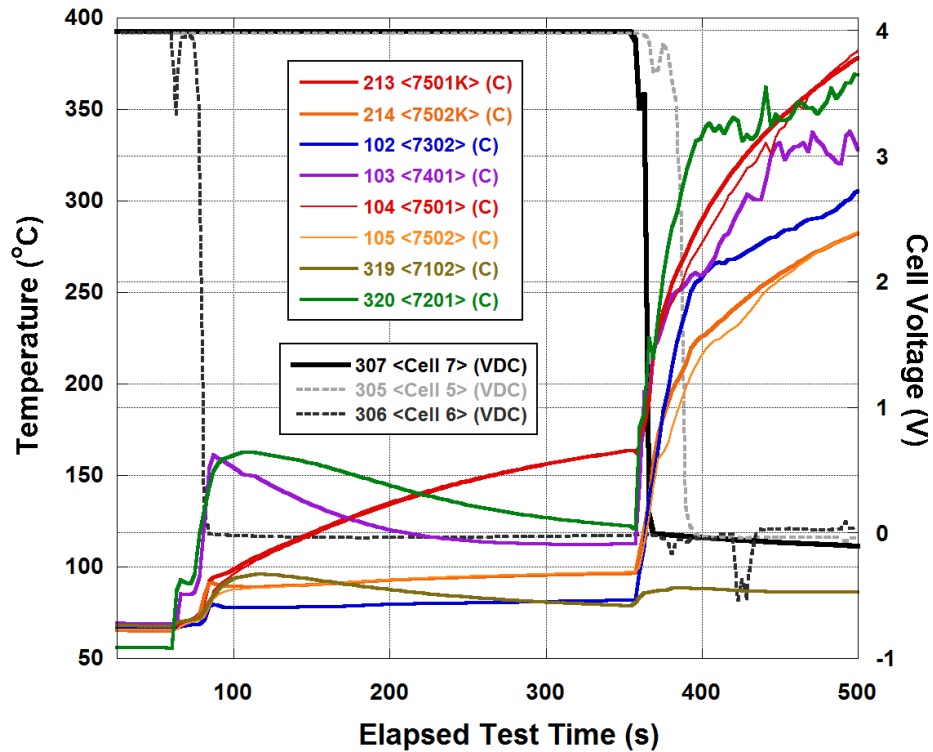


Figure 19. Voltage and temperature data for Cell 7 in the vicinity of the venting event.

Cell 5

Cell 5 was the third cell to vent. The thermocouple data suggest that the venting was triggered by heat energy carried through the positive terminal along the busbar connected to Cell 6, seen in the data from thermocouple 5502. Heat from Cell 6 was also transferred through Face 1 of Cell 5, seen in the temperature rise on thermocouples 5101 and 5102. Some heating was also observed at Face 2 immediately after venting of Cell 6. Thermocouple 5102 shows higher temperatures than 5101 due to the additional heat energy arriving through the busbar connected to Cell 6. After venting, the temperatures on the sides of the cell (Faces 1, 2, and 3) increase in temperature the most. Increased noise on the Type J thermocouples located at sides 2 and 3 after venting suggest that the circuit integrity of these junctions is lost once temperature approaches 500°C. Face 3 remained below 100°C until Cell 5 vented, likely due to its location away from the venting at Cells 6 and 7.

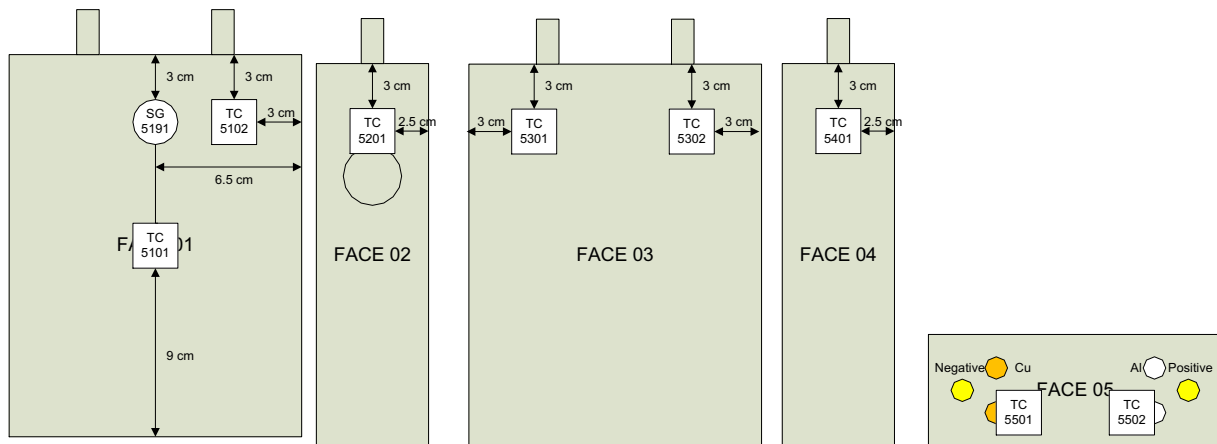


Figure 20. Location of thermocouples attached to Cell 5.

Table 7. Time and temperature data at time of Cell 5 failure.

	Onset of Initial Voltage Drop	Onset of Voltage Drop to Zero	Immediately After Drop to Zero	Maximum Temp.	Time of Maximum Temp. (s)
Test Time (s)	360	381	396		
Time After Nail Penetration	5:00	5:21	5:36		
Type J TC #5101 (°C)	219.5	315.3	416.7	578.3	999
Type J TC #5102 (°C)	197.5	359.9	410.3	566.1	993
Type J TC #5201 (°C)	118.8	265.0	407.9	(630)	1014
Type J TC #5301 (°C)	84.68	114.1	420.2	564.6	1071
Type J TC #5302 (°C)	74.32	316.4	428.5	(690)	1026
Type J TC #5401 (°C)	88.72	160.3	231.2	571.0	1059
Type J TC #5501 (°C)	90.42	126.4	161.8	470.5	1059
Type K TC #5501K (°C)	91.56	127.6	162.0	543.8	1056
Type J TC #5502 (°C)	198.0	207.4	227.0	(490)	1215
Type K TC #5502K (°C)	199.7	211.9	243.2	469.9	1062

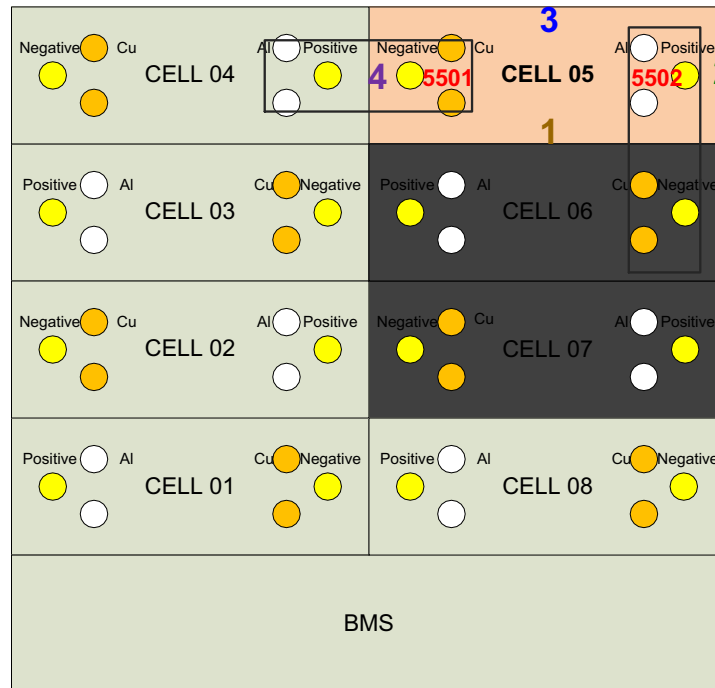


Figure 21. Schematic of the eight cells within the battery, showing location of busbars and designation of each face for Cell 5. Gray shading denotes cells that have previously vented.

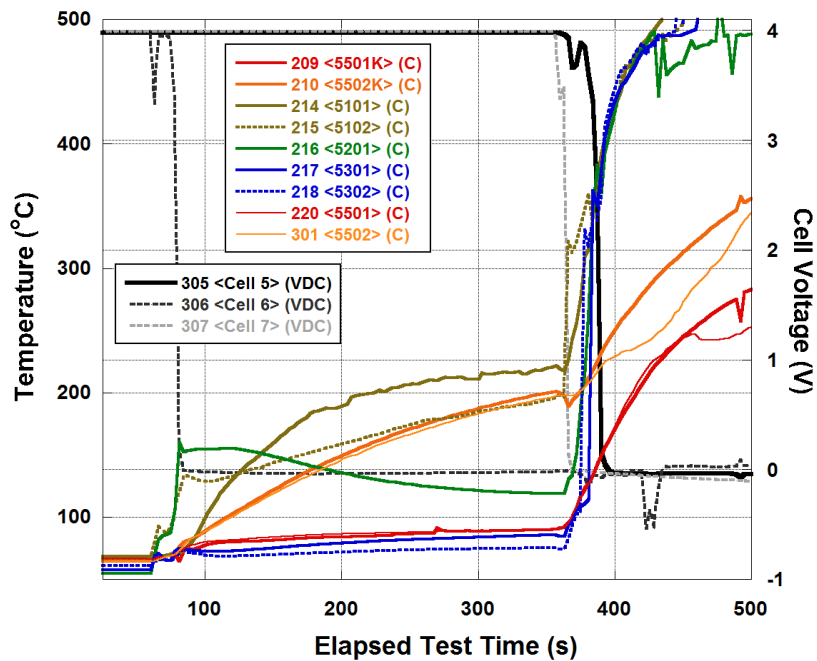


Figure 22. Voltage and temperature data for Cell 5 in the vicinity of the venting event.

Cell 8

Cell 8 vented approximately 250 seconds after the twin venting events at Cells 5 and 7. Cell 8 received a significant amount of heating from the venting of Cell 7. The most significant temperature rise was at Face 2, which is adjacent to the venting hole at Cell 7, rising to almost 400°C immediately after the Cell 7 venting event. It is possible that the increased heating at Cell 8 was due to flow out of the battery enclosure through a large test lead opening near Face 2, Cell 8. Significant heating was observed on Face 3 of Cell 8, which was adjacent to vented Cell 7. Thermocouple 8301 exhibited higher temperatures relative to thermocouple 8302, likely due to the additional heat transferred from the vented exhaust gases escaping along Face 2 of Cell 8 that was released from the vent hole at Cell 7. Heat transfer through the busbar connected between Cells 7 and 8 was also observed, seen in the thermocouple 8502 data.

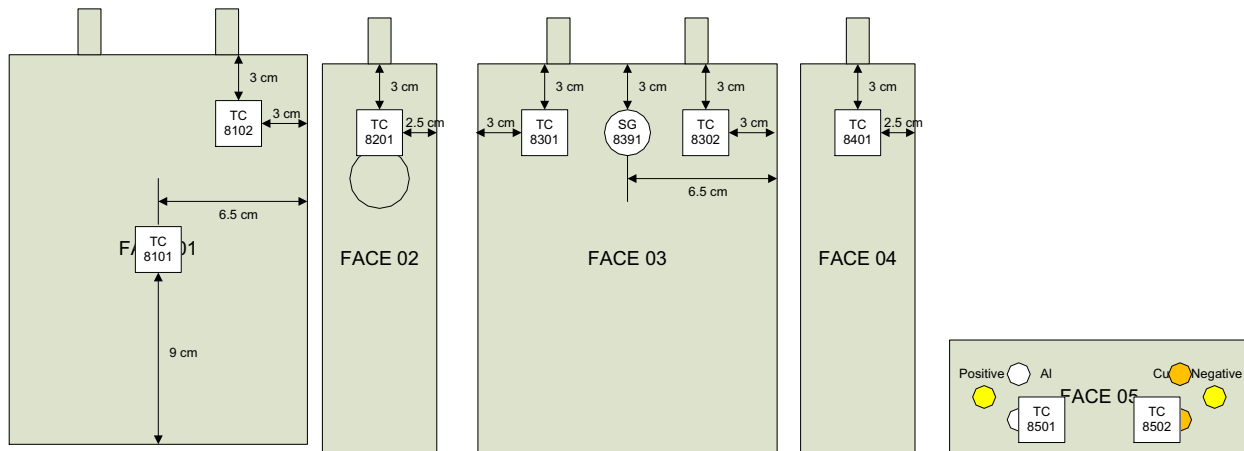


Figure 23. Location of thermocouples attached to Cell 8.

Table 8. Time and temperature data at time of Cell 8 failure.

	Onset of Initial Voltage Drop	Onset of Voltage Drop to Zero	Immediately After Drop to Zero	Maximum Temp.	Time of Maximum Temp. (s)
Test Time (s)	603	612	621		
Time After Nail Penetration	9:03	9:12	9:21		
Type J TC #8101 (°C)	93.43	121.3	258.0	627.1	1155
Type J TC #8102 (°C)	105.2	313.1	-	607.0	1137
Type J TC #8201 (°C)	149.9	310.0	420.7	677.2	690
Type J TC #8301 (°C)	221.6	239.2	424.9	(550)	753
Type J TC #8302 (°C)	201.1	224.9	348.6	611.6	825
Type J TC #8401 (°C)	99.93	168.0	379.0	554.4	1188
Type J TC #8501 (°C)	116.9	120.9	168.6	(590)	1026
Type K TC #8501K (°C)	117.3	127.4	186.6	416.5	1788
Type J TC #8502 (°C)	178.7	180.9	238.7	(440)	834
Type K TC #8502K (°C)	181.6	182.7	261.2	484.4	1152

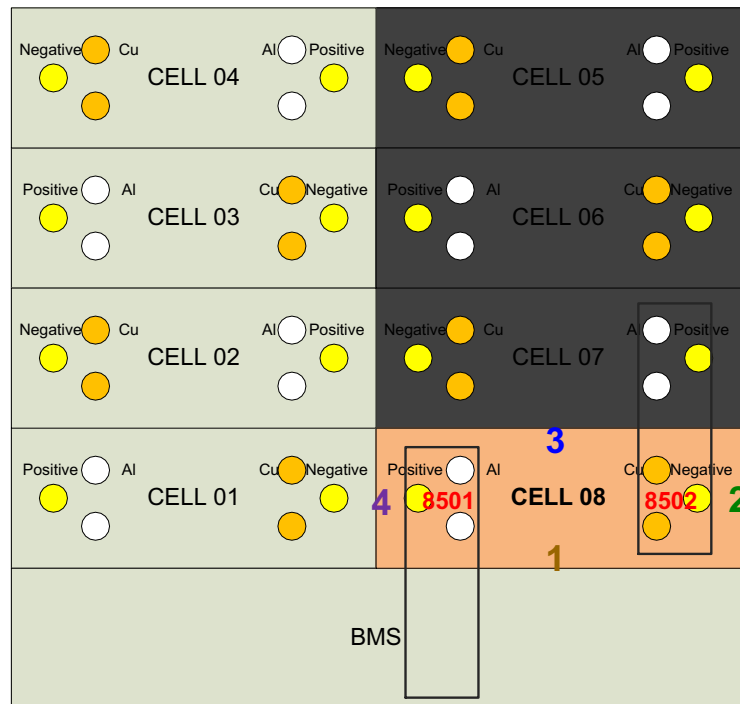


Figure 24. Schematic of the eight cells within the battery, showing location of busbars and designation of each face for Cell 8. Gray shading denotes cells that have previously vented.

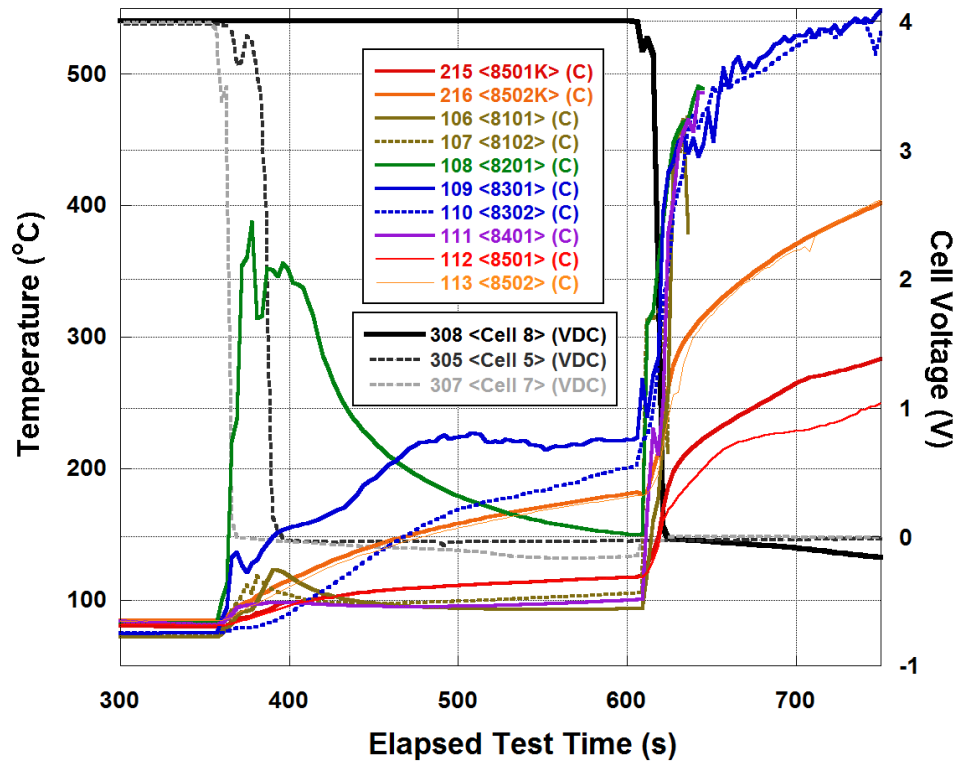


Figure 25. Voltage and temperature data for Cell 8 in the vicinity of the venting event.

Cell 3

Cell 3 was the first cell to vent on the side opposite of the nail penetration event (Cells 1-4). The duration between Cell 8 venting and Cell 3 venting was the longest span of time between any other two venting events (more than 350 seconds). Venting appears to have been caused by heat transfer to Face 4 of Cell 3 from the vented Cell 6, maintaining temperatures at Face 4, Cell 3 above 300°C. Face 3 is also at an elevated temperature, holding above 200°C before Cell 3 vents. It is likely this is heat transferred from the venting events at Cells 7 and 8. The busbar closest to Cell 6 (at thermocouple 3502) shows increased heating, likely as a result of heat traveling Cell 6, possibly through Face 4 and into Cell 3, and then up into the busbar. As with other venting events, heating after venting is most significant at the vent hole on Face 2, as well as significant heating at the busbars leading from the cell. Several Type J thermocouples ceased to operate around the time of venting of Cell 3.

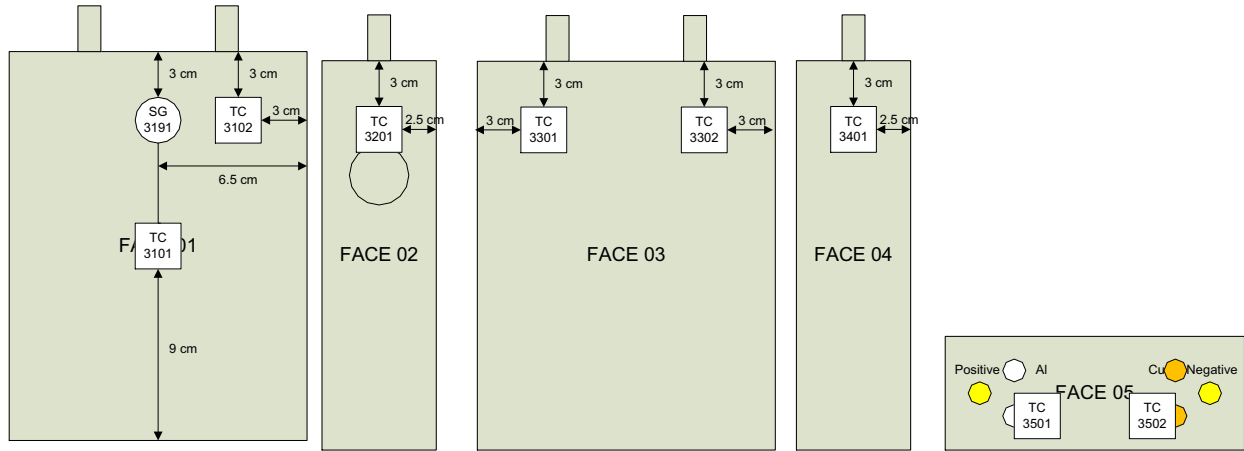


Figure 26. Location of thermocouples attached to Cell 3.

Table 9. Time and temperature data at time of Cell 3 failure.

	Onset of Initial Voltage Drop	Onset of Voltage Drop to Zero	Immediately After Drop to Zero	Maximum Temp.	Time of Maximum Temp. (s)
Test Time (s)	993	999	1002		
Time After Nail Penetration	15:33	15:39	15:42		
Type J TC #3101 (°C)	-	-	-	-	-
Type J TC #3102 (°C)	99.11	138.3	137.6	(560)	1488
Type J TC #3201 (°C)	92.68	-	-	-	-
Type J TC #3301 (°C)	-	-	-	-	-
Type J TC #3302 (°C)	-	-	-	-	-
Type J TC #3401 (°C)	321.5	-	-	-	-
Type J TC #3501 (°C)	-	-	-	-	-
Type K TC #3501K (°C)	113.7	178.3	198.8	664.4	1191
Type J TC #3502 (°C)	-	-	-	-	-
Type K TC #3502K (°C)	212.7	238.6	254.8	533.7	1755

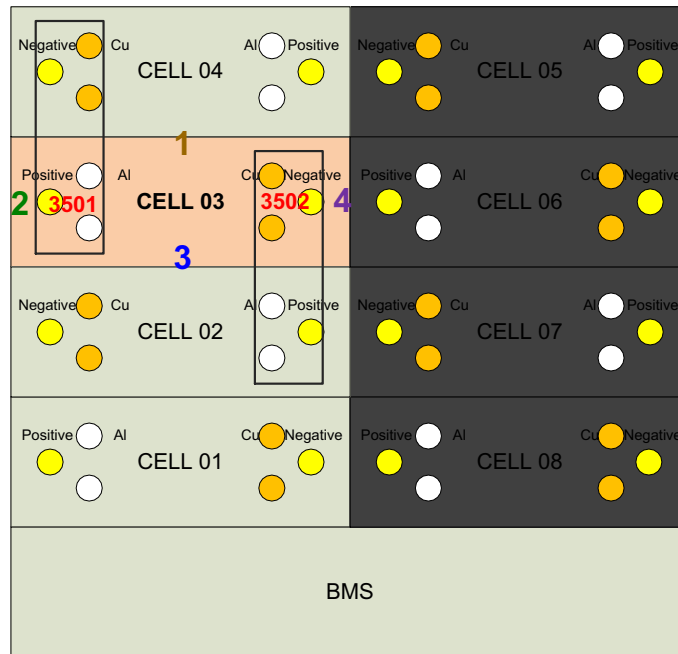


Figure 27. Schematic of the eight cells within the battery, showing location of busbars and designation of each face for Cell 3. Gray shading denotes cells that have previously vented.

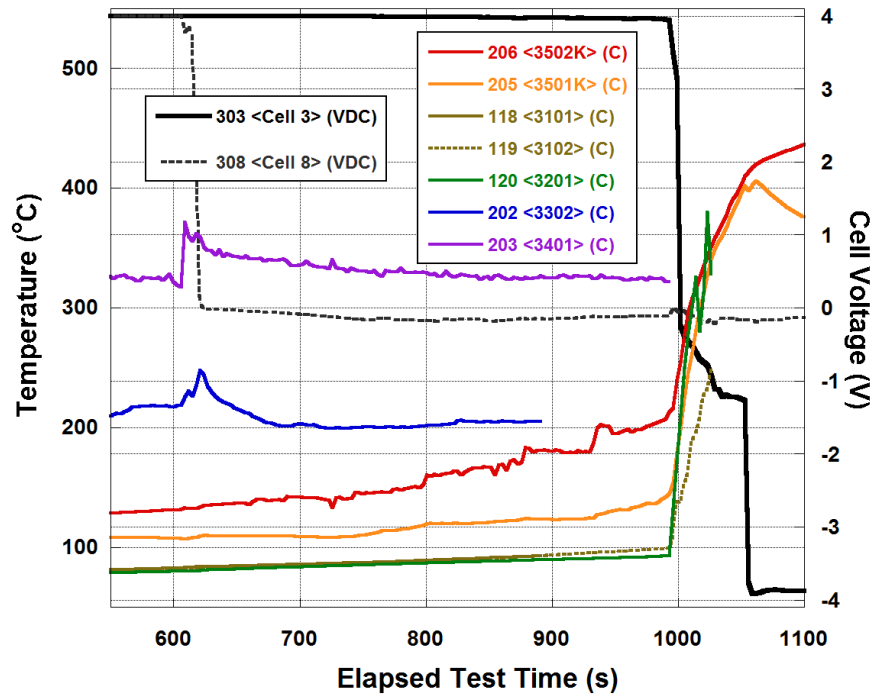


Figure 28. Voltage and temperature data for Cell 3 in the vicinity of the venting event.

Cell 2

After the venting of Cell 3, the two adjacent cells 2 and 4 were triggered into failure as well. Venting of Cell 2 was the first of these two events to occur. Venting was most likely triggered through heat transfer from the vented Cell 7 applied to Face 4 of Cell 2, which was nearly 400°C several minutes before the Cell 2 venting event. Additional heat energy was applied immediately after the venting of Cell 3 at Face 1 closest to the vent hole on Face 2, Cell 3. Since the temperature rise closer to the vent hole (thermocouple 2102) was much higher than that observed at the center of Face 1 (thermocouple 2101), it is concluded that the heat source was centered around the venting event through the vent hole of Cell 3. It is possible that the applied temperature at thermocouple 2102 rose much higher than the peak at 480°C, as the temperature data is reminiscent of a damaged thermocouple. The lower rise in temperature on Face 2 suggests that the vented gases from Cell 3 did not pass along Face 2 of Cell 2, and that most of the heat transfer from the venting event was from cell case to cell case. As with the other cells, the temperatures of the cell sides 1-4 rose at a faster rate than that observed at the busbars. As in other venting events, several of the Type J thermocouples ceased to operate several seconds after the venting event.

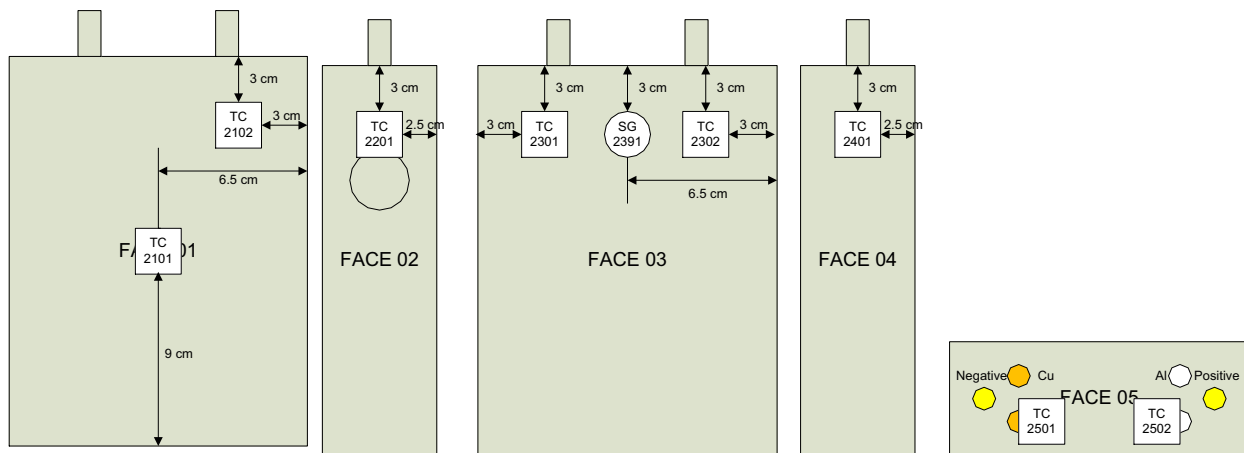


Figure 29. Location of thermocouples attached to Cell 2.



Table 10. Time and temperature data at time of Cell 2 failure.

	Onset of Initial Voltage Drop	Onset of Voltage Drop to Zero	Immediately After Drop to Zero	Maximum Temp.	Time of Maximum Temp. (s)
Test Time (s)	1152	1158	1161		
Time After Nail Penetration	18:12	18:18	18:21		
Type J TC #2101 (°C)	284.5	293.1	331.8	(610)	1470
Type J TC #2102 (°C)	339.2	331.0	329.1	(680)	1473
Type J TC #2201 (°C)	166.0	244.1	381.3	583.9	1458
Type J TC #2301 (°C)	115.9	142.2	166.1	584.5	1761
Type J TC #2302 (°C)	178.1	190.2	190.1	577.5	1410
Type J TC #2401 (°C)	407.6	442.3	453.8	(590)	1638
Type J TC #2501 (°C)	147.7	166.5	184.9	510.6	1863
Type K TC #2501K (°C)	145.9	165.6	193.5	527.6	1944
Type J TC #2502 (°C)	249.3	256.4	-	-	-
Type K TC #2502K (°C)	261.6	269.2	285.7	527.6	1962

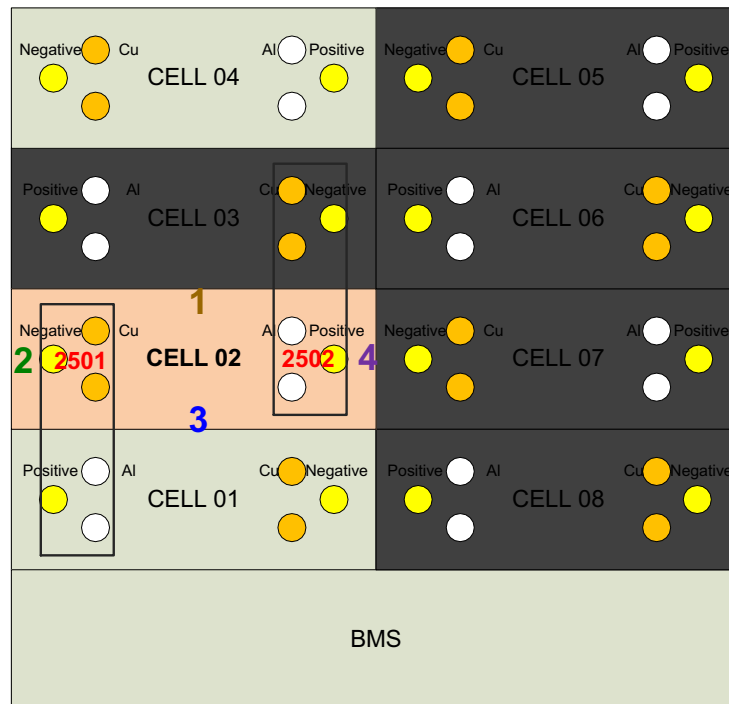


Figure 30. Schematic of the eight cells within the battery, showing location of busbars and designation of each face for Cell 2. Gray shading denotes cells that have previously vented.

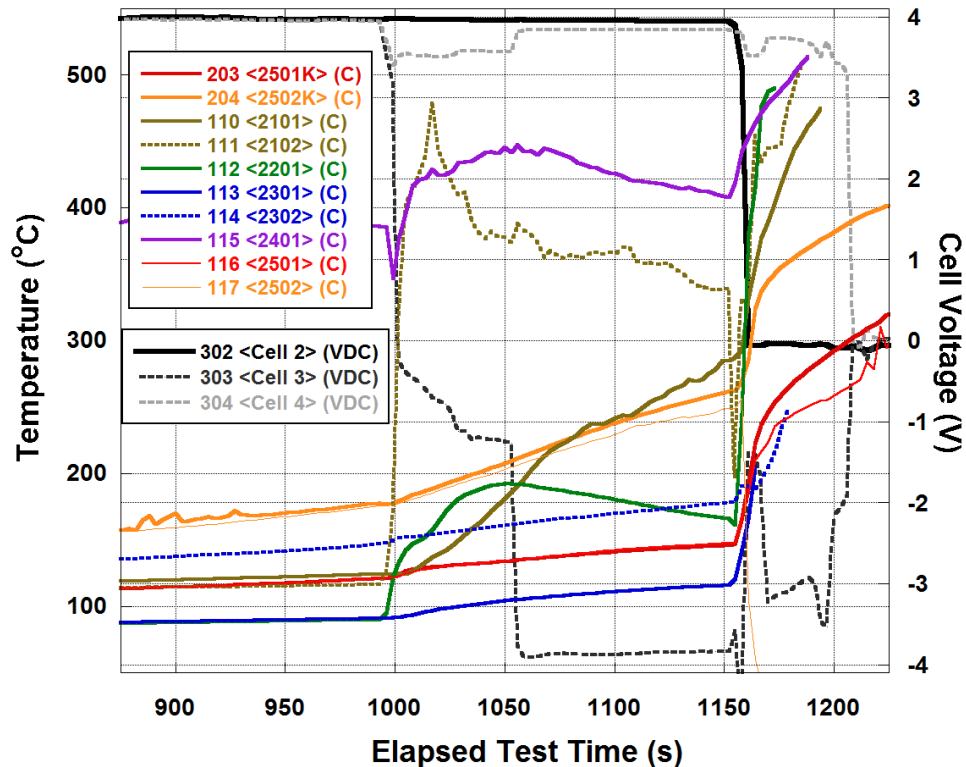


Figure 31. Voltage and temperature data for Cell 2 in the vicinity of the venting event.

Cell 4

Like the venting of Cells 5 and 7, Cells 2 and 4 were twin venting events triggered by an adjacent venting cell (Cell 3). However, the thermal and electrical data from Cell 4 suggest that venting was triggered through (at least in part) by external shorting of the cell. Significant heating from the previously vented Cell 5 is also observed at Face 4 (thermocouple 4401), with sustained temperatures above 300°C measured. This heating shows a marked increase immediately following venting of Cell 3.

Aside from the heating from Cell 5, significant temperature rise is observed along Face 1, which is facing away from the other cells. Additionally, the thermocouples on Face 3 are not showing significant response to the venting of the adjacent Cell 3. This suggests a combination of one or more of the three following scenarios:

- The thermocouples on Faces 1 and 3 were switched during installation, so that thermal data from Face 3 is shown instead as coming from Face 1.



- The thermocouples on Face 3 were damaged earlier, which is supported by the significant noise in the signal, and failure of thermocouples 4301 and 4302 before the venting of Cell 4. Therefore, heating is not observable on Face 3.
- Significant heating is occurring along Face 1 due to the short-circuit path to the battery case. This high-current scenario may also have contributed to internal self-heating and subsequent venting of Cell 4.

By the time of venting of Cell 4, much of the Type J thermocouples had been damaged. This is observable in the noisy and incomplete temperature data shown in Figure 34. The spikes in temperature measured during the moment of Cell 4 venting are also suspect, possibly due to continuity issues of the thermocouple wires during the event.

Observation of this heating located away from Cell 3 and the drop in cell voltage on Cell 4 at this time, it is likely that significant current draw was occurring from Cell 4 at the time immediately following venting of Cell 3. This high-current path would start at the positive terminal of Cell 4, pass through the vented (and shorted) Cell 5, through the battery case, through the vented (and shorted) Cell 3, and then to the negative terminal of Cell 4. This high-current scenario is supported by the significant voltage drop observed on Cell 4 immediately after venting of Cell 3, when this short-circuit path would have been formed. The significant rise in temperature on the busbar between Cells 4 and 5 suggests that much of the voltage drop occurred at this interconnect.

It appears that one of the three internal sub-cells within Cell 4 fails quickly during the venting of Cell 3 (observed by the drop and fast recovery of the cell voltage). This failure and the proposed location of the other two sub-cell failures are marked by arrows and numbered 1-3 in Figure 34. After this time a high-current scenario is observed, with Cell 4 voltage being pulled to around 3.5V and significant heating is observed on Faces 1, 4, and the busbar between Cells 4 and 5. This fault appears to clear itself after about one minute, with cell voltage returning to a higher value (though visibly lowered due to high current draw, to around 3.7V), and cell temperatures begin to cool at Faces 4 and 5. This clearing appears to be attributed to Cell 3, since the change in Cell 4 behavior is reflected in a significant change in the measured Cell 3 voltage. The reverse biasing of Cell 3 suggests that the fault is “cleared” through the formation of an elevated resistive path between the terminals of Cell 3, probably consisting of carbonized material in the cell interior. The short from the negative terminal of Cell 3 to the battery case likely remains, with the reverse biasing being provided due to +4V applied from Cell 2 to the negative terminal of Cell 3. This reverse biasing disappears once Cell 2 begins to vent, but is partially re-established once Cell 2 carbonizes and reverts to a resistive state, transferring the biasing from the still-intact Cell 1.

Additional heat energy was transferred across the busbar from Cell 3 to Cell 4 after venting of Cell 3 (observed on thermocouple 4501). This transfer of heat increased further after the venting of Cell 2. This heat transfer may have contributed to triggering the venting of Cell 4.

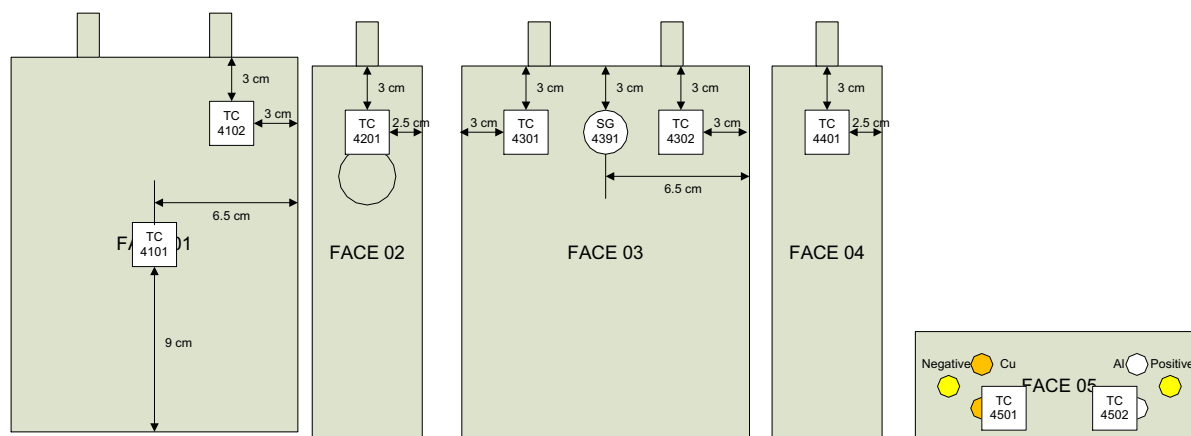


Figure 32. Location of thermocouples attached to Cell 4.

Table 11. Time and temperature data at time of Cell 4 failure.

	Onset of Sub-Cell 1 Voltage Drop	Onset of Sub-Cell 2 Voltage Drop	Onset of Voltage Drop to Zero (Failure of Sub-Cell 3)	Immediately After Drop to Zero	Max Temp.	Time of Max Temp. (s)
Test Time (s)	996	1185	1200	1209		
Time After Nail Penetration	15:36	18:45	19:00	19:09		
Type J TC #4101 (°C)	93.35	278.4	322.9	(567)	(690)	1212
Type J TC #4102 (°C)	157.8	334.2	304.5	(741)	(741)	1209
Type J TC #4201 (°C)	114.0	-	-	-	-	-
Type J TC #4301 (°C)	121.1	-	-	-	-	-
Type J TC #4302 (°C)	111.3	-	-	-	-	-
Type J TC #4401 (°C)	309.2	311.2	276.3	-	-	-
Type J TC #4501 (°C)	113.1	222.8	234.2	244.6	770.4	1377
Type K TC #4501K (°C)	118.1	239.3	239.9	253.6	504.4	1872
Type J TC #4502 (°C)	252.9	288.9	258.8	293.2	427.8	1641
Type K TC #4502K (°C)	260.5	296.2	267.4	286.8	490.9	1818

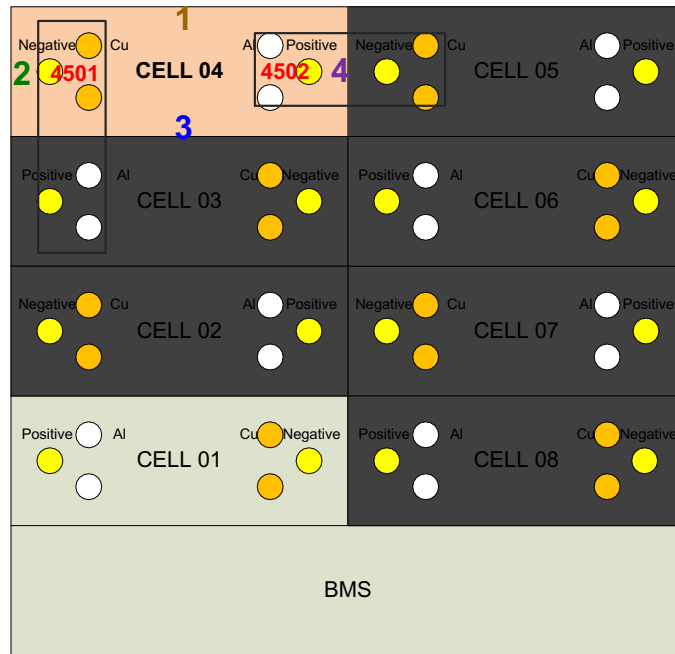


Figure 33. Schematic of the eight cells within the battery, showing location of busbars and designation of each face for Cell 4. Gray shading denotes cells that have previously vented.

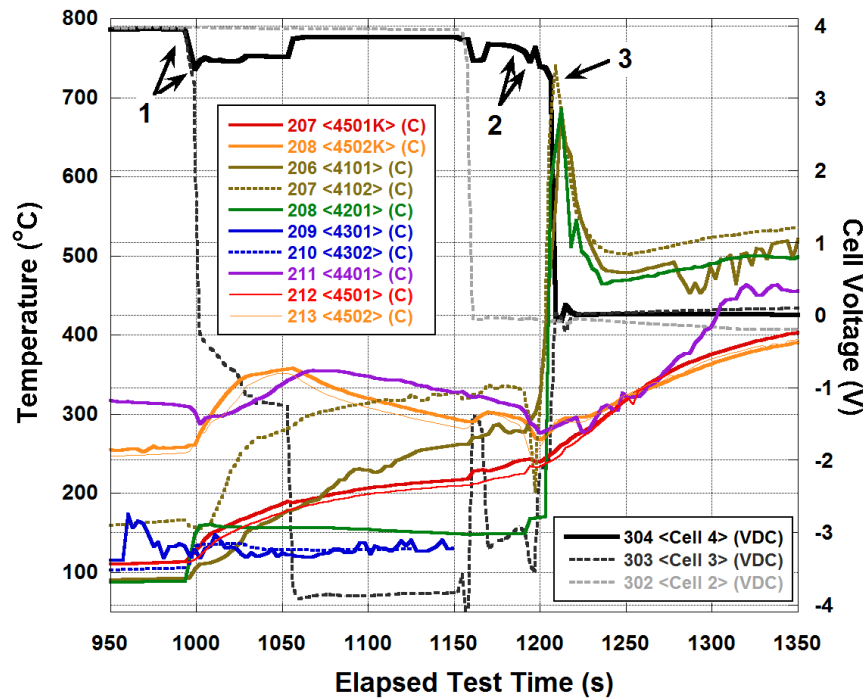


Figure 34. Voltage and temperature data for Cell 4 in the vicinity of the venting event.

Cell 1

The last cell to vent was Cell 1. The voltage sense lead for Cell 1 failed soon after the test began, so time of failure on this cell is estimated through observation of thermal measurements and voltage measurements across the battery. The temperature data suggest that venting of Cell 1 was induced through heat transfer to Face 1 of Cell 1 from the vented Cell 2. This is supported by the significant temperature rise observed on thermocouples 1101 and 1102. As in the case of prior cells, the temperature on Face 1 closest to Face 2 is significantly higher (more than 50°C) than at the face center, suggesting that much of the heat energy from the venting of Cell 2 was centered near the vent hole (and therefore Face 2). Since thermocouple 1401 was not responsive at the time of the venting event, it is not known to what extent heat transfer from the vented Cell 8 to Face 4 of Cell 1 contributed to the venting event. A small drop in temperature was observed immediately prior to the venting of Cell 1. The source of this is not understood at this time. It is unlikely attributed to electrical current flow, since the negative terminal of Cell 1 was at open circuit and the other cells were at zero volts at the time of the cooling event. It is possible this is a result of cessation of Cell 4 providing current to short-circuit pathways, but the data are insufficient to fully explain the nature of this cooling effect.

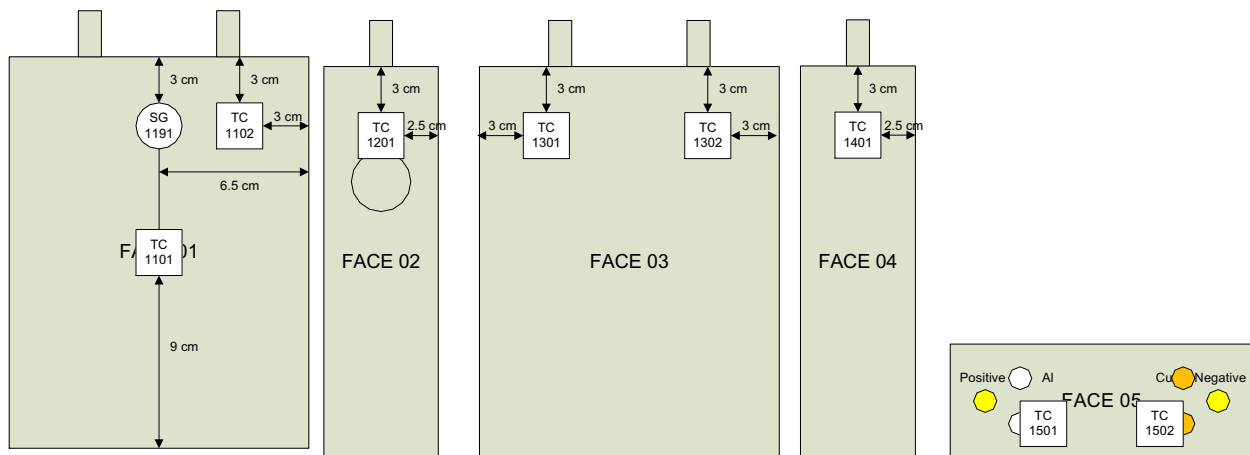


Figure 35. Location of thermocouples attached to Cell 1.



Final Report for 787 Battery (Asset 436) Tested at 70°C, Ungrounded

Table 12. Time and temperature data at time of Cell 1 failure.

	Onset of Initial Voltage Drop	Onset of Voltage Drop to Zero	Immediately After Drop to Zero	Maximum Temp.	Time of Maximum Temp. (s)
Test Time (s)	1209	1215	1221		
Time After Nail Penetration	19:09	19:15	19:21		
Type J TC #1101 (°C)	173.2	160.9	201.8	554.6	1734
Type J TC #1102 (°C)	236.9	257.8	401.8	525.5	1731
Type J TC #1201 (°C)	-	-	-	-	-
Type J TC #1301 (°C)	178.8	206.0	336.3	553.9	1830
Type J TC #1302 (°C)	208.0	293.2	296.0	614.4	1452
Type J TC #1401 (°C)	-	-	-	-	-
Type J TC #1501 (°C)	181.8	194.5	218.2	510.3	1791
Type K TC #1501K (°C)	185.4	184.9	220.0		
Type J TC #1502 (°C)	230.0	229.9	238.3	496.8	1797
Type K TC #1502K (°C)	235.5	228.1	247.2		

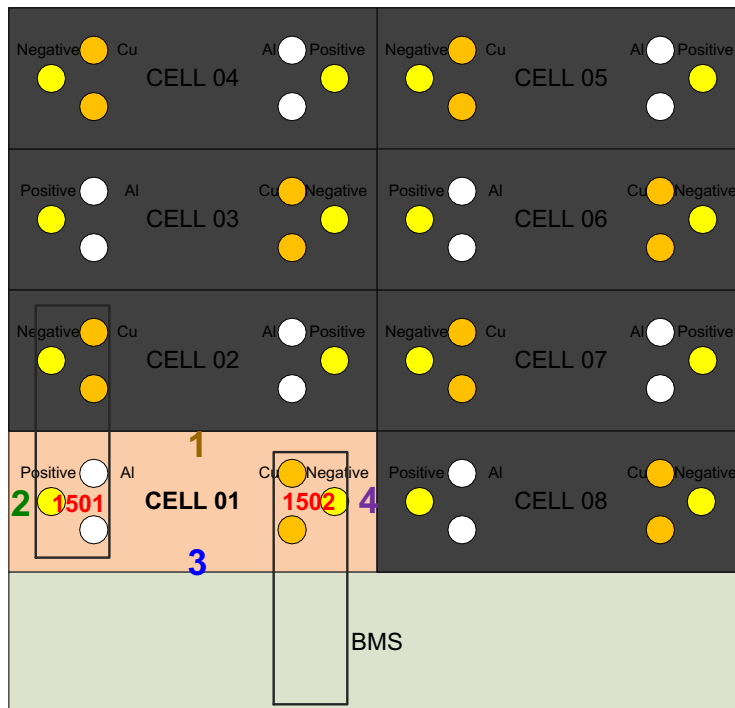


Figure 36. Schematic of the eight cells within the battery, showing location of busbars and designation of each face for Cell 1. Gray shading denotes cells that have previously vented.

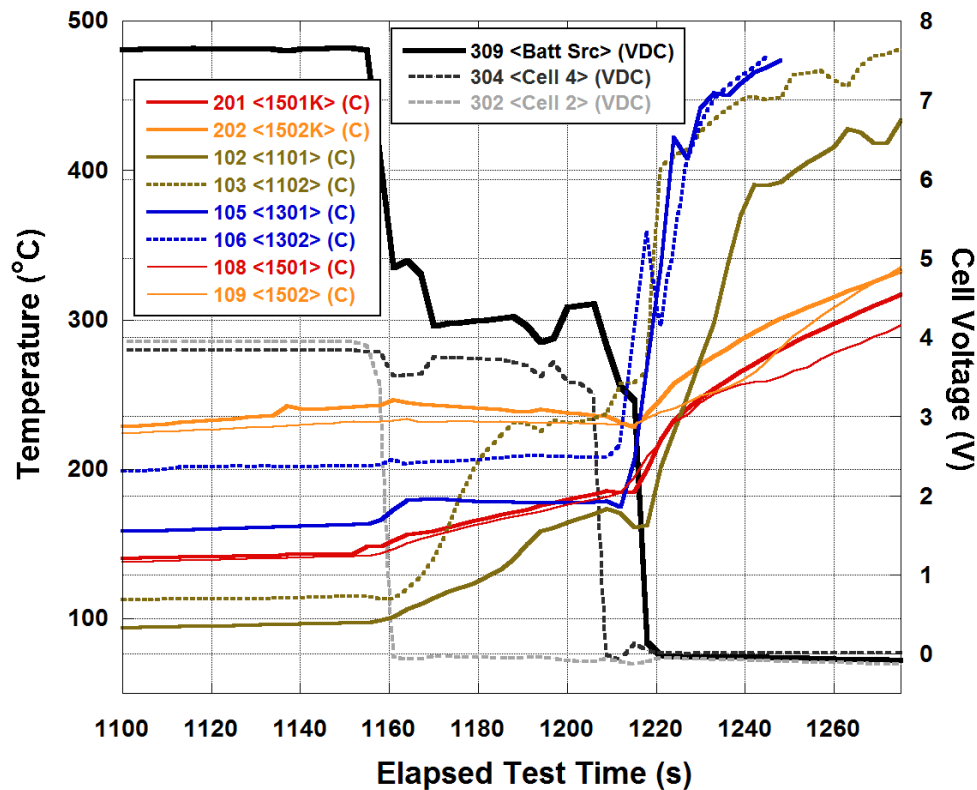


Figure 37. Voltage and temperature data for Cell 1 in the vicinity of the venting event.

Battery Voltage and Ground

The voltages across each cell are shown in Figure 38, along with the measured battery output voltage. This plot can be compared to the voltage potential at the ground terminal, which gives the potential of the case (referenced to the negative terminal of the battery), shown in Figure 39. Immediately following the venting of Cell 6, the case ground is biased to 20V, which shows that Cell 6 shorts to the case, connecting the positive output of Cell 5 to the case (which is at 20V relative to the negative terminal of the battery). Once Cell 5 vents, this potential drops to 16V, the potential across Cells 1 through 4. It is not clear whether Cell 5 shorts to the case or whether the connection is made through Cell 6. Venting of Cell 3 cuts this bias further, to 8V, the potential across Cells 1 and 2, and suggests Cell 3 shorts to the case (as Cell 4 is intact at this point in the test). Discharging of Cell 4 is seen as a slight elevation of the case voltage, as it contributes some voltage through Cell 3 during discharge. This is also observed in the reversal of voltage potential across Cell 3 during discharging of Cell 4 through the case short. The case potential then drops to 8V once the Cell 4 discharging event stops. The case potential continues to fall to 4V after Cell 2 vents and 0V once Cell 1 vents.

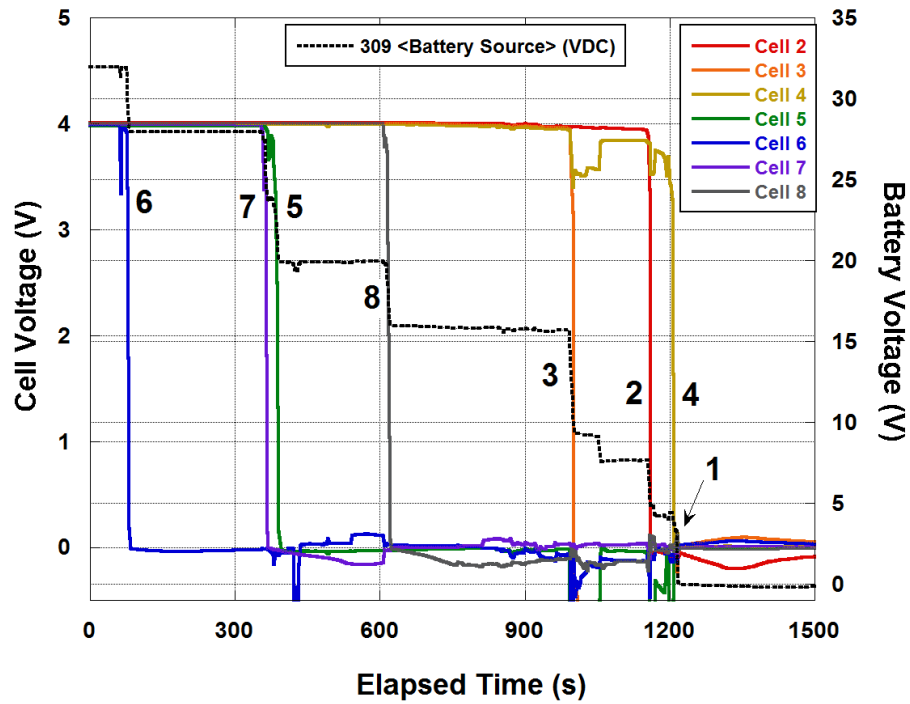


Figure 38. Plot of cell voltages and battery voltage, measured through entire test.

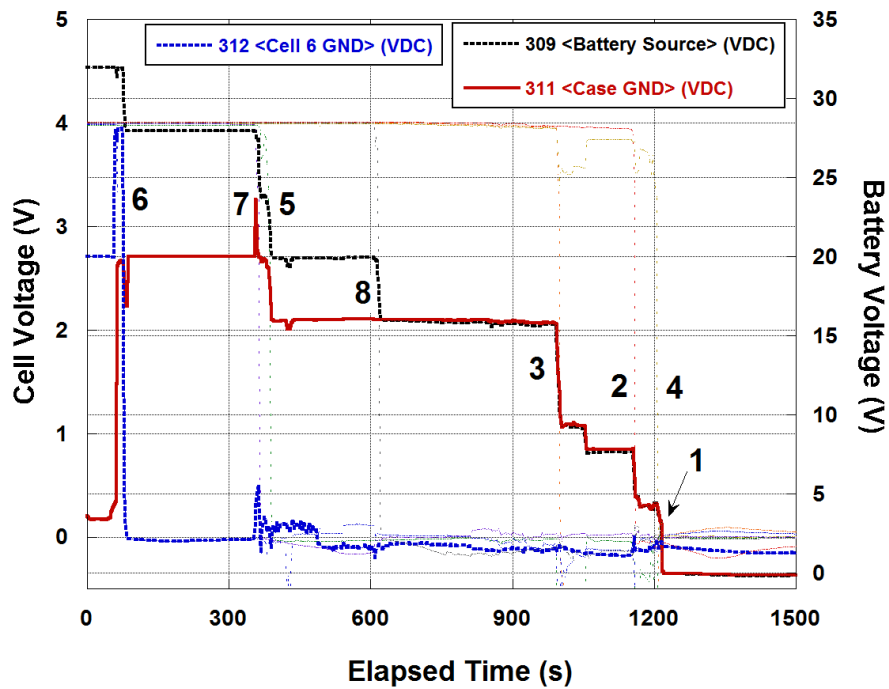


Figure 39. Plot of battery voltage, with case ground voltage and Cell 6 case voltage shown.

Spectral Analysis

Through the duration of the test, 740 files of 100 ms each were recorded every 3.6 seconds, capturing the time-domain voltage across Cell 6. The voltage was sampled at 10 MS/s (10^7 samples per second, or 1 million samples over 100 ms), each sample with a resolution of 18 bits. These files were then processed using automated LabVIEW-based software to calculate two FFT spectra, using 50,000 points for each spectrum.

One of the spectra was generated by first filtering the raw waveform through a digital low-pass filter (10-order Butterworth filter with -3 dB point at 250 kHz). This is then decimated by a factor of 20 to a 50,000-point waveform (decimating done by averaging each group of 20 datapoints to generate a single, averaged datapoint for the decimated file). The waveform is then passed through a Hanning window and the FFT is calculated. The resulting spectrum gives 10 Hz resolution to a maximum value of 250 kHz.

The second spectrum is generated by breaking the 100 ms waveform into twenty segments of 5 ms each. Each of these segments is passed through a Hanning filter and the FFT is calculated for each. These twenty spectra are then averaged together to give an average spectrum for the twenty segments. This method reduces the effect of random noise and preserves resolution at the highest frequencies. Resulting spectra have 200 Hz resolution to a maximum frequency of 5 MHz.

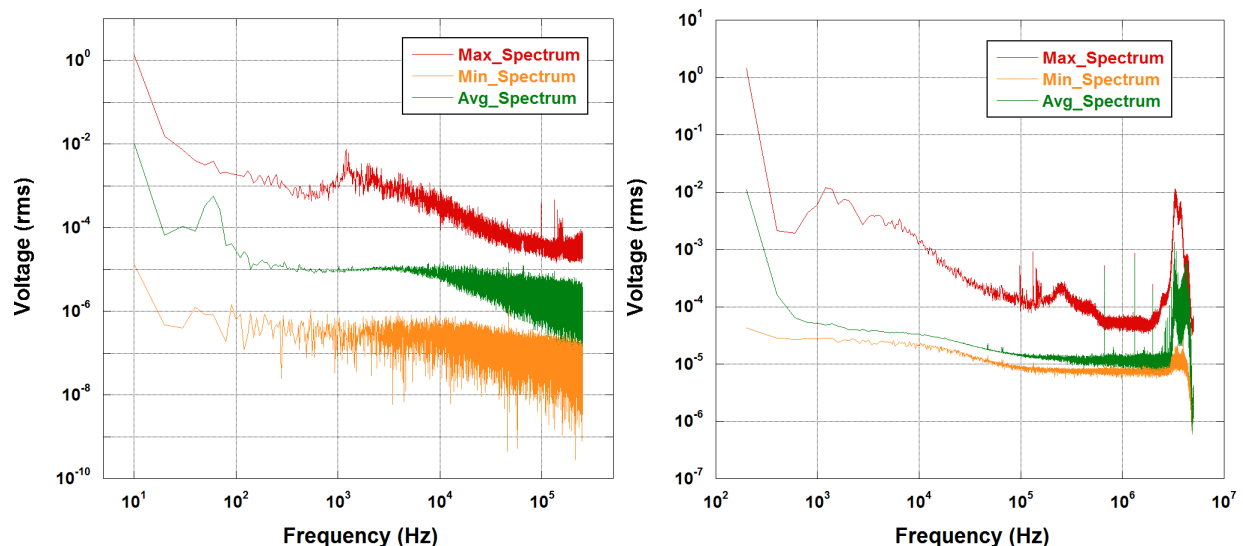


Figure 40. Maximum, minimum, and average spectral values recorded over the duration of the test. (Left) Sampled at 500 kS/s with 10 Hz resolution. (Right) Sampled at 10 MS/s with 200 Hz resolution.

The entire set of 740 spectra is then analyzed to obtain the maximum, minimum, and average at each frequency value. The maximum value at each frequency is recorded so that spectra containing the highest spectral components can be easily identified and retrieved for further analysis. The maximum, minimum, and average values are shown in Figure 40. The maximum curves above 1 kHz reflect a $1/f^2$ power law relationship, which is reminiscent of arcing behavior. As this is a composite graph capturing the maximum values from all 740 spectrum plots, it is desirable to identify which files captured the most significant events. This is achievable by plotting the file number for which each maximum frequency component was recorded, and then evaluate those files where the maximum values were recorded most. This is graphed in Figure 41. As can be seen, maximum values tend to be concentrated in a relatively small number of files, suggesting that relatively significant wideband events are occurring at these moments in time.

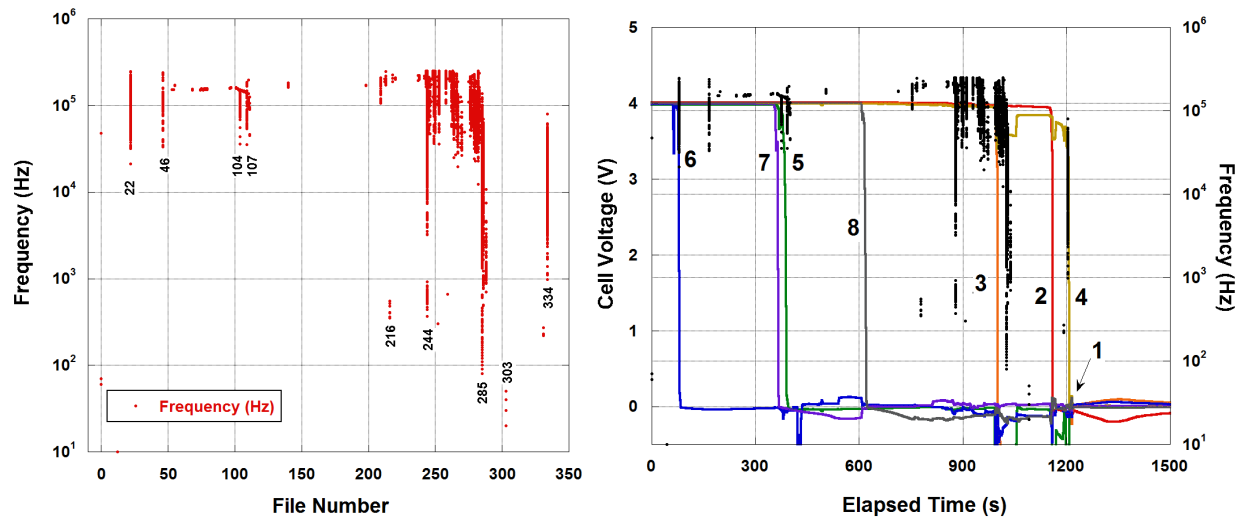


Figure 41. Location with respect to (left) file number and (right) test time of maximum amplitude for each of the 50,000 frequencies tracked in each of the 740 spectral files. At right the data are superimposed onto cell voltage data. Left plot lists file numbers with the most significant number of recorded maxima.

Figure 42 shows four example spectral plots from two events containing significant spectral content. Figure 42 (left) shows the spectral content during (File 22) and after (File 46) nail penetration and subsequent venting of Cell 6. This is compared to the open-circuit spectrum (the spectrum taken when no test leads are connected to the instrument) and the spectrum at the start of test before nail penetration. Spectral noise appears to increase by approximately one order of magnitude during the nail penetration event, possibly signifying the presence of electrical arcing. The $1/f^2$ relationship above 1 kHz is consistent with previously observed arcing behavior; the flattened response below 1 kHz does suggest presence of wideband noise, but has more of a “white noise” characteristic which has not been observed in previously

observed arcing behavior. However, shorting effects as the battery interior carbonizes may be a source of this lower-frequency suppression of expected arcing magnitude.

The most significant wideband noise was observed within File 285, captured during the high-current discharge of Cell 4 (Figure 42, *right*). In this case the $1/f^2$ pattern is more apparent above 1 kHz and the overall spectral magnitude increased by a factor of 100 (+20 dB) above that measured before the nail penetration event.

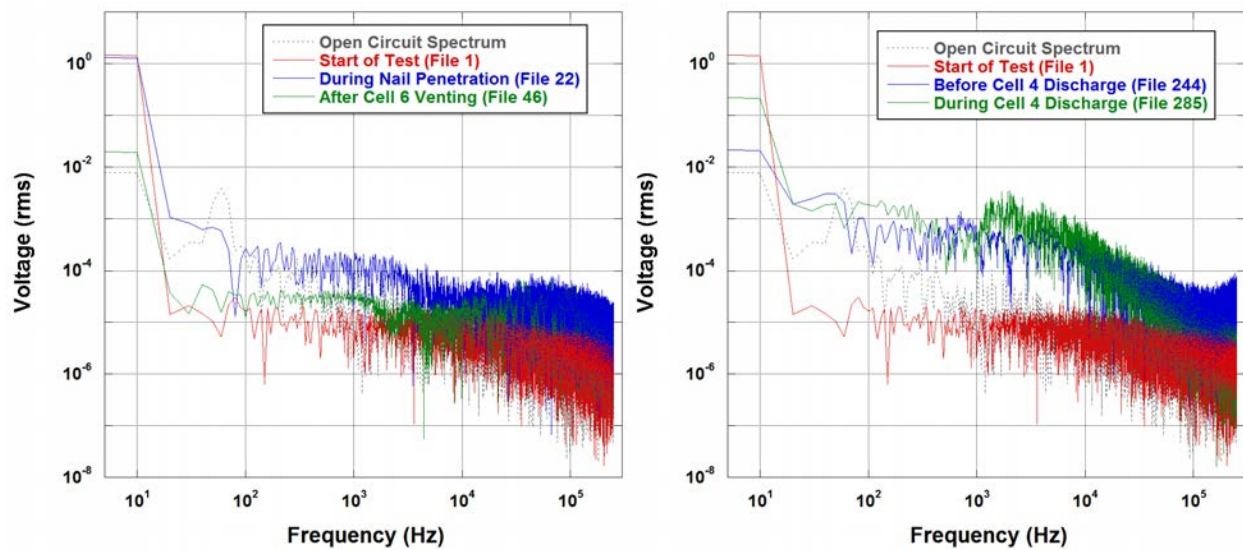


Figure 42. Spectra identified to have significant maximum frequency components. (*Left*) Spectra during and after Cell 6 venting (files 22 and 46). (*Right*) Spectra before and during Cell 4 rapid discharge event (Files 244 and 285, respectively). Open-circuit (prior to connection to battery terminals) and start-of-test spectra are also shown for comparison.

The spectra can be fit to a power law relationship, which can be used to give an anticipated spectral magnitude at any given frequency. Figure 43 shows such a fit for File 285, which was recorded during the high-current discharge event of Cell 4, and represented the waveform with the most spectral content recorded during the entire test. The fit matches well within the kHz range, deviating from the expected trend at lower frequencies (which may be an effect due to carbonization and resultant shorting across the Cell 6 terminals). This power law fit can be expressed as the following:

$$V_{rms}(f) \approx 203 \cdot f^{-1.31}$$

The spectrum above 250 kHz fell below the noise floor of the measurement and was subject to instrument noise-related artifacts. However, prior characterization experience of electrical arcing events suggests that this $1/f^2$ power law relationship would continue to represent spectral content of arcing at higher frequencies should measurement capabilities allow for its characterization.

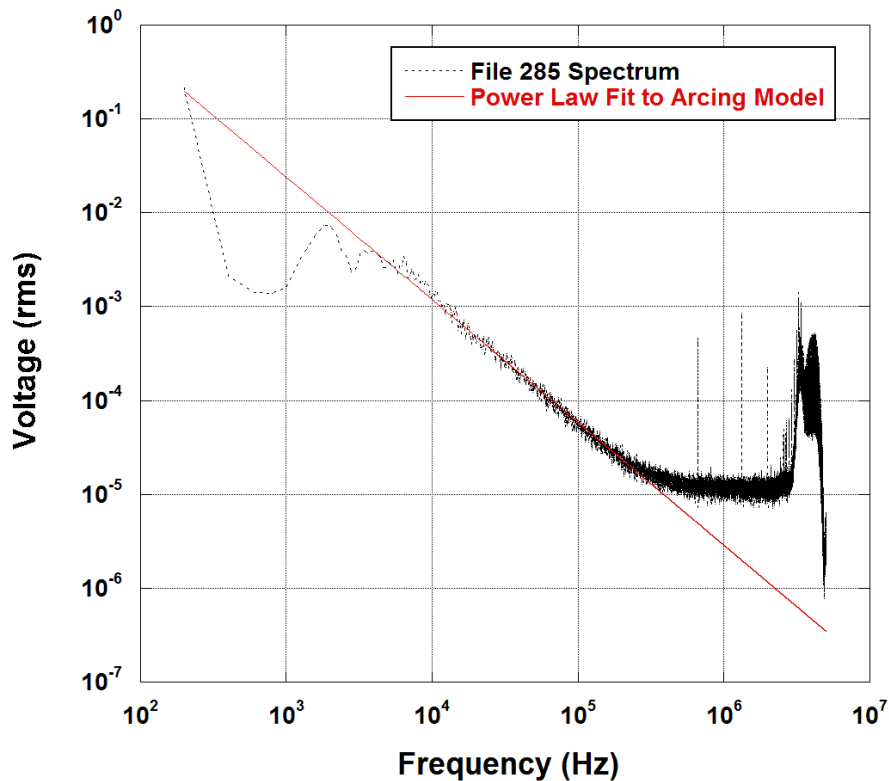


Figure 43. Power law fit to spectral data observed during Cell 4 discharging event (File 285), showing agreement with power law fit that is consistent with electrical arcing behavior. Flattening and artifacts above 250 kHz are result of noise floor and equipment noise, respectively.

Summary of Electrical and Thermal Testing

The battery was held at 70°C for several hours inside an environmental chamber. At the initiation of testing, the battery internal temperature ranged between approximately 66°C and 68°C. A nail was driven into the center of Face 5 of Cell 6, forming an internal short circuit of the cell and therefore triggering a venting event. Thermal energy from this venting event is then transferred to Cells 5 and 7, causing twin venting events. The thermal data suggest that the most likely mechanism of heat transfer was through the



busbars connected to Cell 6. Heat was then transferred to Cell 8, primarily through the flow of hot gases venting from Cell 7 across Face 2 of Cell 8, as well as transfer to the body of Cell 8 through Face 3, which was adjacent to Face 7. Cell 8 then vented, completing venting of all four cells on one side of the battery. After the longest delay between venting events (250 seconds), Cell 3 vents through heat transfer from Cell 6 to the adjacent Face 4 of Cell 3. After Cell 3 vents, a short-circuit is formed across Cell 4, resulting in rapid discharge of Cell 4 and heating on its Face 1 (which is adjacent to the battery case and the likely short circuit path). At the same time, Cell 2 vents due to heat transfer from the vented Cells 3 and 7 through adjacent faces. Cell 4 then vents, heated both from thermal transfer from the venting of Cell 3, as well as Joule heating due to shorting of Cell 4 through Cells 3 and 5 to the battery case. This additional heating is observed on Face 1 and the positive terminal busbar connected to Cell 5 (at this time, the battery case is biased at 4V, causing much of the voltage drop to appear across the positive busbar on Cell 4). Cell 1 is then the last cell to vent, triggered through thermal transfer from Cell 2 and (likely) Cell 8.

The high-frequency data were analyzed using automated software, which collected statistical information on the recorded spectra. The evaluation shows several potential occurrences of electrical arcing, though the spectral content below 1 kHz was observed to be less than would be expected. The most significant spectral content was observed during the high-current discharge of Cell 4, with the observable power law relationship suggesting that spectral noise originates as arcing. A power law fit suggests that the spectral noise from arcing voltage falls off with respect to frequency at a rate of -13 dB/decade and arcing power is expected to diminish at -26 dB/decade.

Post Test Disassembly

The battery was disassembled after discharging the cells. The photographic documentation of the disassembled battery is presented in Appendix A. Figure 44 shows the locations of each melted/open collector within each cell. It was observed that only aluminum electrodes melted/opened during the test; all copper electrodes remained intact. The pattern of openings suggests that the sub-cell to fail first results in opening of that electrode. For example, the center sub-cell on Cell 6 shows an opened electrode, which reflects the fact that the center electrode was the one driven to failure due to nail penetration. After Cell 6 failure, heat transfer from venting transferred to Cell 7, resulting in its failure. As can be seen, the sub-cell electrode within Cell 7 located closest to Cell 6 exhibits the melted/opened electrode. This is also true with Cell 8, which vented due to heat transfer from Cell 7, and also shows opened electrodes closest to Cell 7. This is also observed in Cells 2 and 4, which both vented as a result of heat transfer from Cell 3.

This pattern of failure suggests the failure mechanism as shown in Figure 45, and the corresponding voltage behavior is shown in Figure 46. In this model, heat transferred to the cell (e.g., from a previously

vented cell) causes one of the three sub-cells to short circuit and draw large current from the rest of the cell. This causes the aluminum electrodes to overheat and open on the cell which is in a short-circuit condition. During short-circuit the voltage of the cell drops, but then recovers once the shorted cell is removed from the circuit. The heat from the failed sub-cell then transfers to the other two sub-cells, causing thermal runaway for the rest of the cell and drop of the cell voltage to zero. This failure model suggests that the electrodes that fused open will denote the sub-cell which failed first, and is expected to help in determining the sequence of cell failure by signaling the direction of heat flow into the cell which caused failure. This also suggests that open electrodes at the center sub-cell suggests that heating originated from within the cell rather than from an adjacent cell, increasing the probability that the cell showing open electrodes at the center sub-cell only was the cell that was first to fail and triggered the entire failure event.

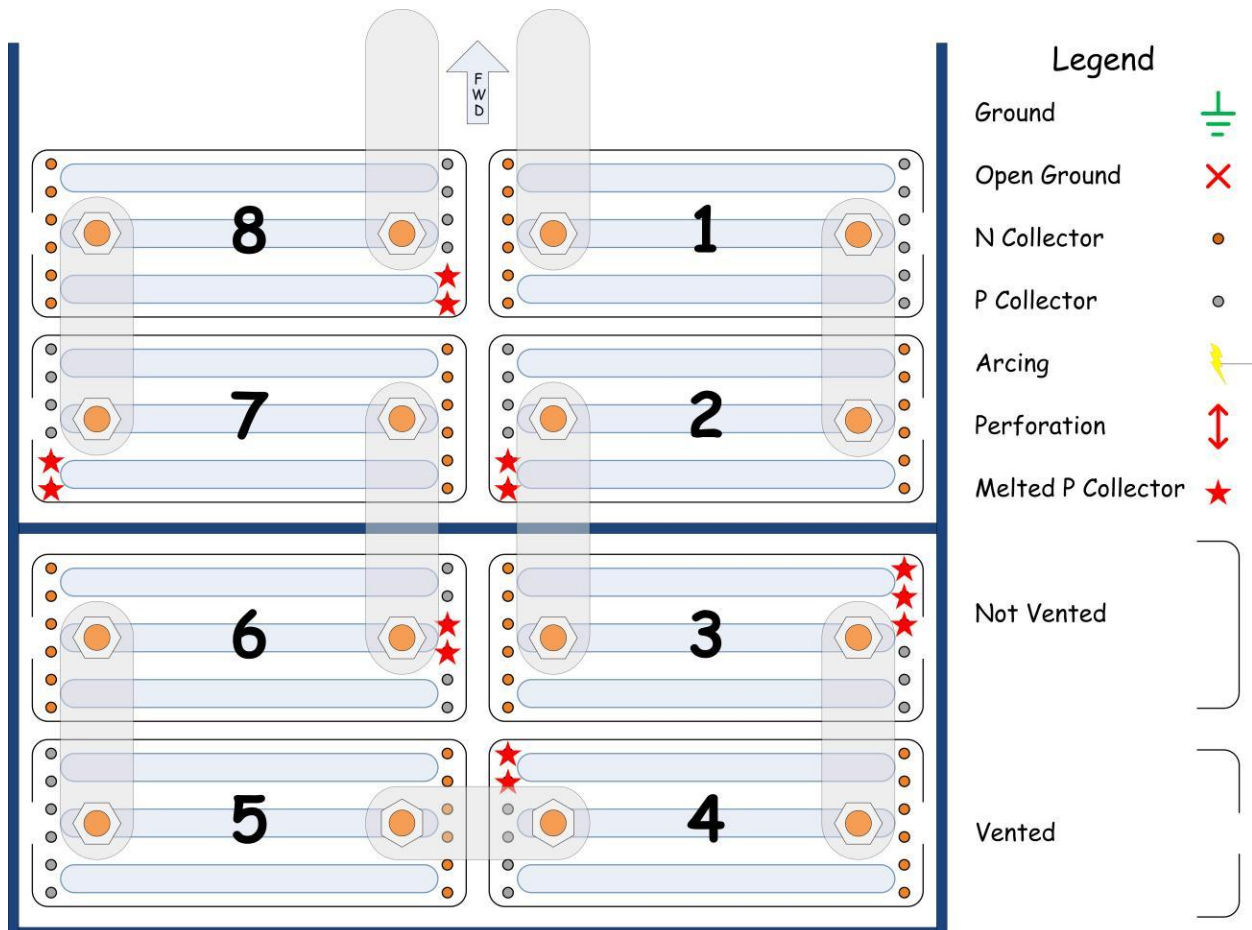


Figure 44. Locations of melted/open collectors inside each battery cell.

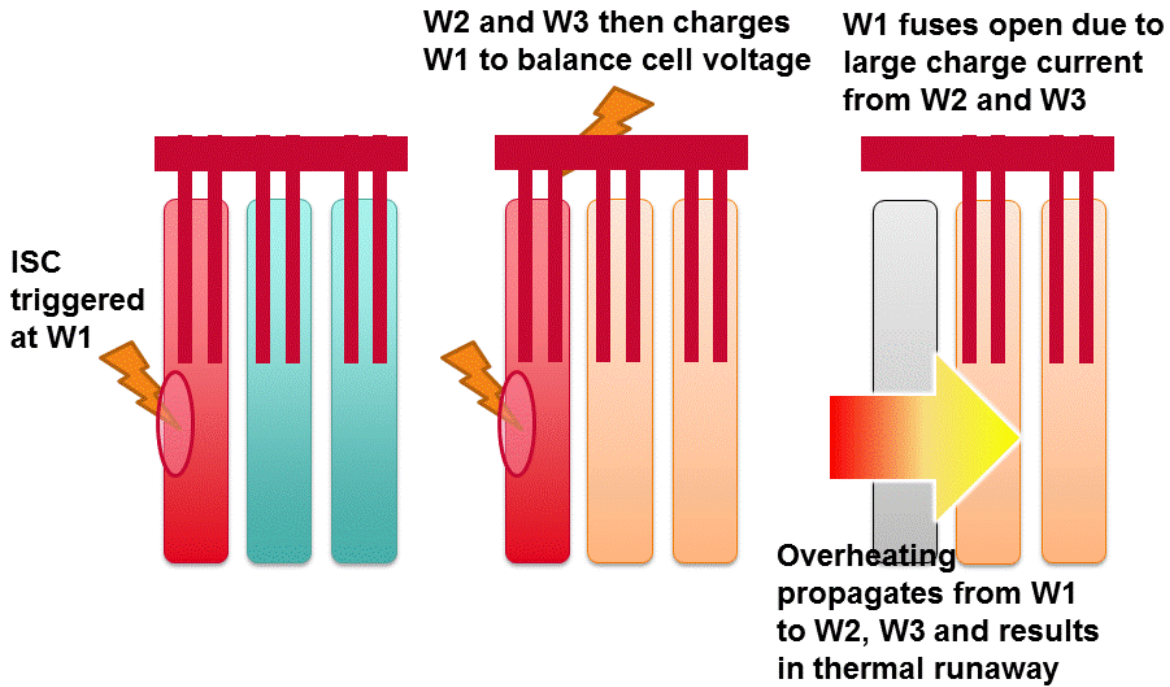


Figure 45. Proposed failure mechanism for cells.

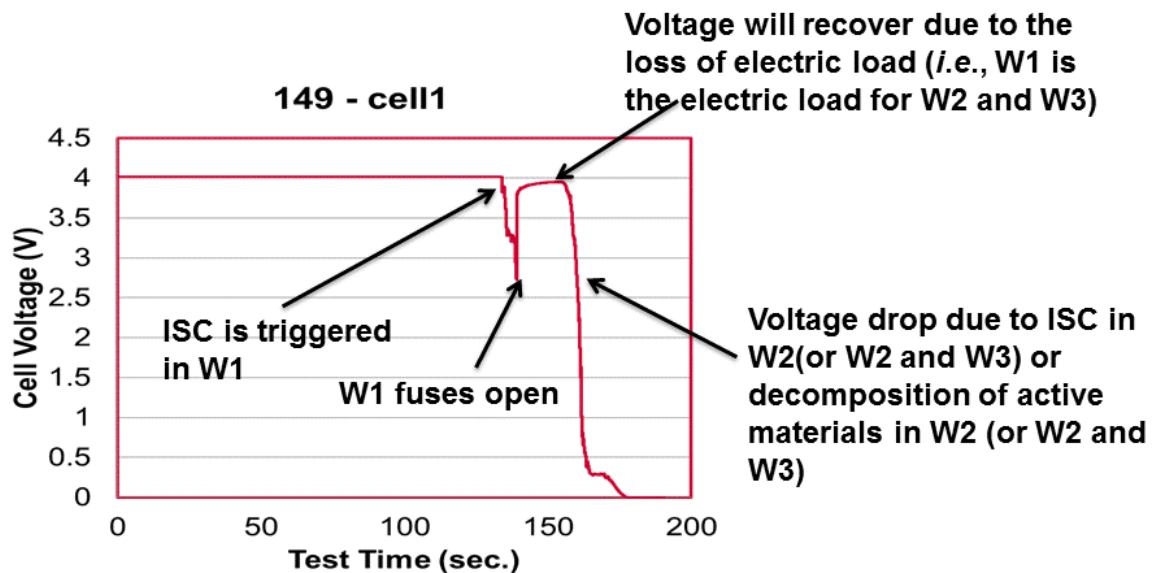
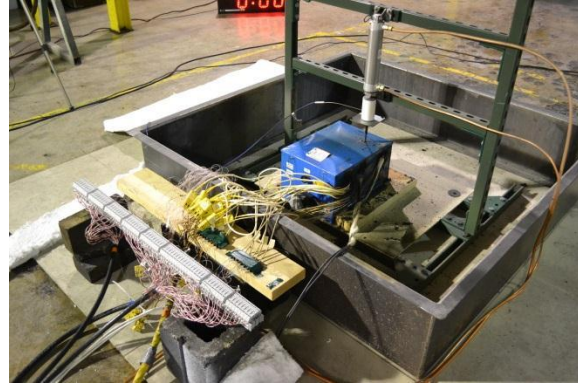
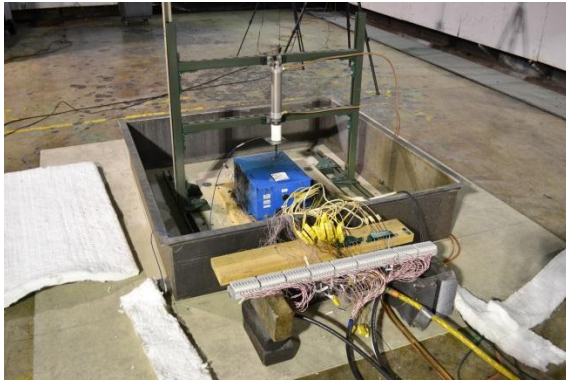


Figure 46. Cell voltage behavior during failure mechanism as shown in Figure 45.



APPENDIX A – POST-TEST DISASSEMBLY PHOTOS

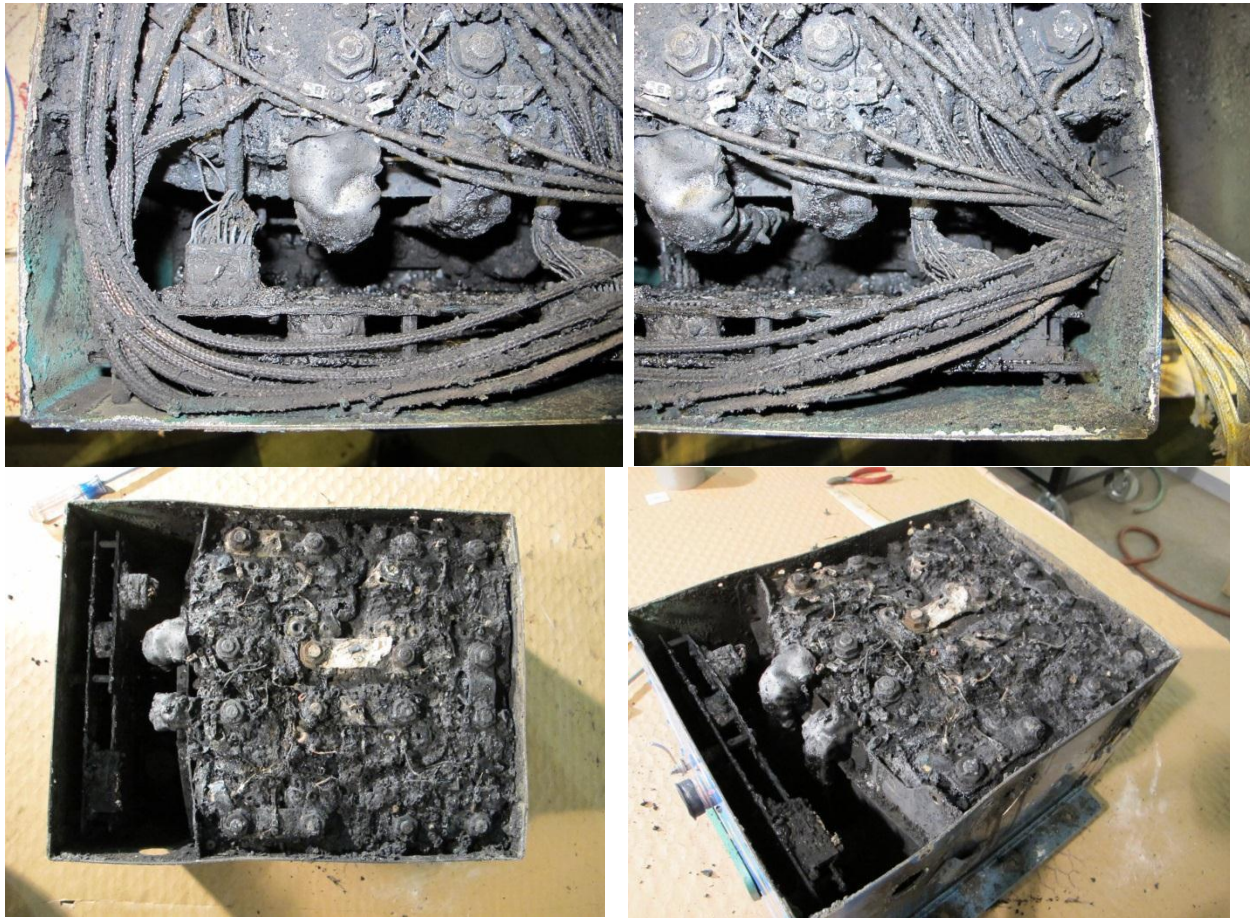
Post- Test Photos – Nail Penetration Apparatus and Intact Battery





Post Test Disassembly Photos – Top of Battery





Intact Battery Post Test Disassembly Photos – Cell Removal



Top of cells

Cells 8, 7, 6 and 5 vent side (l to r)



Cells 5 and 4 (l to r)



Cells 4, 3, 2 and 1 (l to r)



Cells 2, 1 (l to r)



Cells 4, 3 (l to r)



Cells 6, 5 (l to r)



Cells 8, 7 (l to r) b



Cells 4, 3, 2 and 1 (l to r)



Cells 2 and 1 (l to r)



Cells 4 and 3 (l to r)



Cell 3 header



Cells 8, 7, 6 and 5 (l to r)



Cells 6 and 5 (l to r)



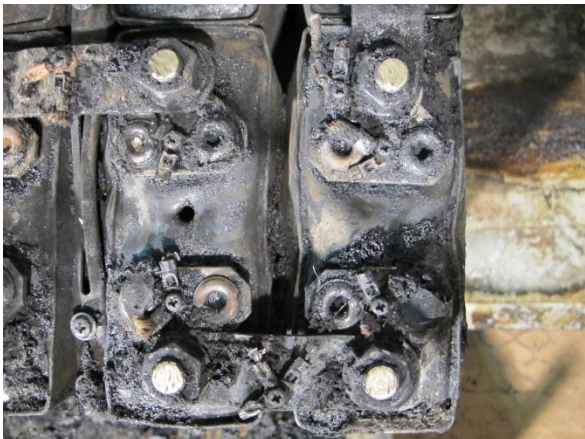
Cells 8 and 7 (l to r)



Cell 1 and 2 header



Cell 3 and 4 header



Cell 5 and 6 header



Cell 7 and 8 header



Cell 6 header (location of NPT)



Cell headers 5, 6, 7 and 8



Cell 5 welded to Cell XX



Cell 5 case breach



Cell 5 case breach



Cell 5 case breach



Cells 5 and 6 welded together



Cells 5 damage



Cell 1 damage



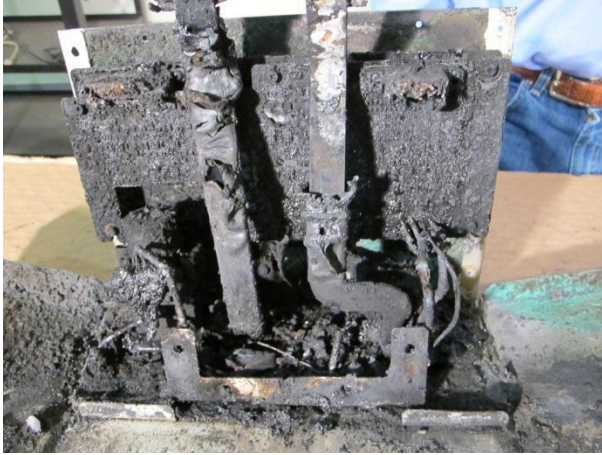
Cell 1 damage



Cell 1 damage



Cell 1 damage



Battery BMU compartment



Battery case disassembled



Battery Post Test Disassembly Photos – Cell 1







Battery Post Test Disassembly Photos – Cell 2







Battery Post Test Disassembly Photos – Cell 3







Battery Post Test Disassembly Photos – Cell 4







Battery Post Test Disassembly Photos – Cell 5







Battery Post Test Disassembly Photos – Cell 6









Battery Post Test Disassembly Photos – Cell 7









Battery Post Test Disassembly Photos – Cell 8







APPENDIX B – BATTERY PRE-TEST DISASSEMBLY ANALYSIS

- Battery Part Number: B3856-901
- Battery Serial Number: 436
- Ambient Temperature at Examination: 75.38°F
- Humidity at Examination: 41%
- Start Time: 14:10
- Stop Time: 15:10
- Total Time: 1 hr

Internal Battery Disassembly



Caution: Electrostatic Discharge Sensitive protection is required.

WARNING! Full battery voltage potential is present!

Personal protective equipment is required.

Remove the cover. Take picture of internal battery and record photo # 436_0870.

Tape the edge of box before start. Numbering of the cells and bus bars occurs clockwise.

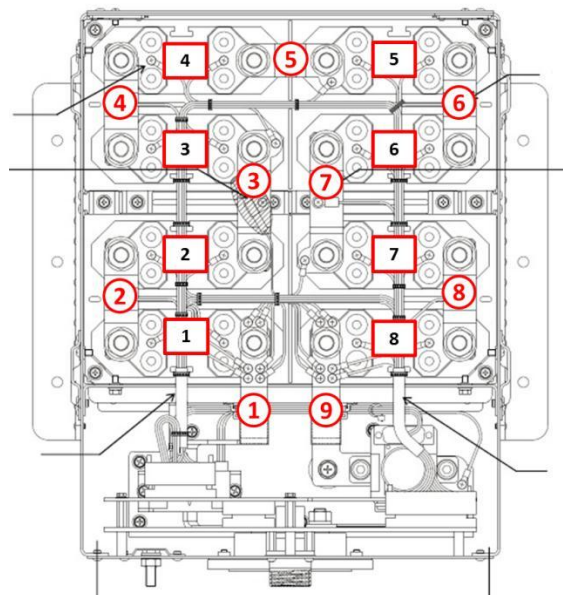


Figure 47. Numbering of the cells and bus bar

Remove the screw of wire “33-A”, “43-I” and “39-F”; put the wire in plastic sleeves.

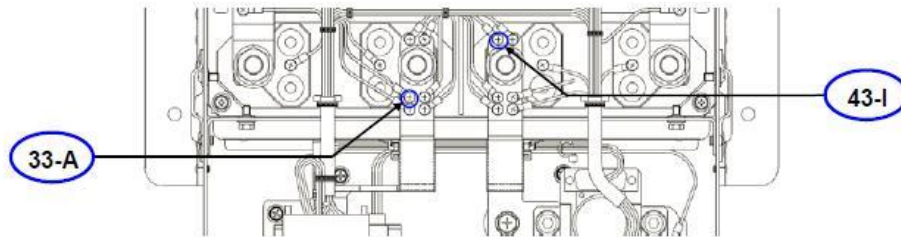


Figure 48. Terminal positions “No. 43-I” and “No. 33-A” of Sub Harness

Put a sheet on cell and disconnect the Sub Harness (210), then disconnect the Main Harness (160). Cut the cable tie and tape the harness on the outside of box.

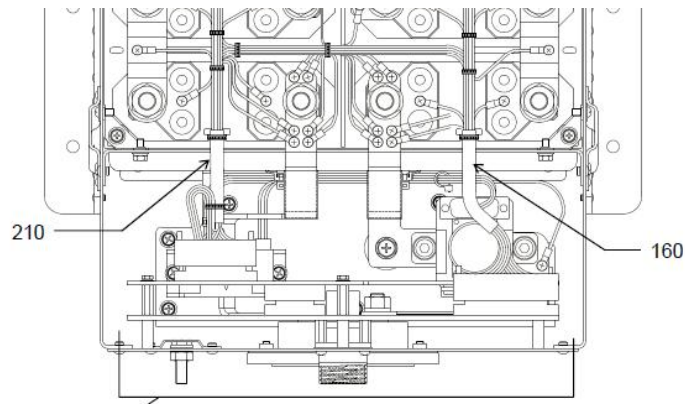


Figure 49. Positions of Sub Harness (210) and Main Harness (160)

Disconnect the HECS contactor harness (360) with wood stick.

Remove the screw of wire “38-E” and put sleeve.

Loose the nuts on bus bar No. 5 and remove it, put sleeve on terminals.

Unscrew the screws on four corners in the outside box to avoid arcing.

Remove the screws on each bus bar and put sleeve on No. 7.

Unscrew the nuts of each bus bar and remove bars, put sleeve on terminals.

Visual observation of bus bar after removes it, take photo if anything unusual.



Bus Bar Observation

Bus Bar No	Inspection Results
2	Normal
3	Normal
4	Normal
5	Normal
6	Normal
7	Normal
8	Normal

Unscrew all screws on each cell and cut cable tie, then remove the whole wire.

Loosen nuts of Positive and Negative bar, bending the bars toward side and put sleeve on terminals.

Unscrew and remove the corner metal fitting.

Unscrew and remove the fixation frame above cells.

Measure OCV.

Equipment Documentation

Equipment	Model	Property Number	Calibration Date
TRUE RMA MULTIMETER	Fluke 289	21120134	2013-09-23



OCV Measurement

Cell #	Results			
	V1 (V)	V2 (V)	V1-V2 (mV)	V1-V2>20mV (Y/N?)
1	3.6894	3.6931	-3.7	N
2	3.6910	3.6945	-3.5	N
3	3.6894	3.6930	-3.6	N
4	3.6918	3.6951	-3.3	N
5	3.6904	3.6937	-3.3	N
6	3.6915	3.6949	-3.4	N
7	3.6903	3.6938	-3.5	N
8	3.6911	3.6942	-3.1	N

Take cell and insulation plates and spacers out. Visual observation and record any unusual phenomena.

Cell Observations

Item	Inspection Results
Cell 1	Normal
Cell 2	Normal
Cell 3	Normal
Cell 4	Normal
Cell 5	Normal
Cell 6	Normal
Cell 7	Normal
Cell 8	Normal
Others	Contamination/residue on cell insulation cover around cell 5~cell 8
Others	Contamination/residue on plastic spacer
Others	Contamination/residue on cell insulation cover around cell 1~cell 4

Measure and record the dimension and weight of each cell.



Equipment Documentation

Equipment	Model	Property Number	Calibration Date
Vernier Caliper	Mitutoyo CD-6" CSX	CAS 413	2013-02-26

Cell Dimension and Weight Measurement

Battery S/N	Cell #	Cell S/N	Weight (g)	Dimension (mm)
436	1	53800044 A	2735.12	Depth (D) (+)Up.: 50.98
				D (+)Mid.: 50.85
				D (+)Lo.: 50.13
				D(-)Up.: 51.09
				D(-)Mid.: 50.79
				D(-)Lo.: 50.00
				Length (L) Up.: 133.31
				L Mid.: 133.29
				L Lo.: 132.09
				Height (H) (+):177
				H(-): 177



Final Report for 787 Battery (Asset 436) Tested at 70°C, Ungrounded

Battery S/N	Cell #	Cell S/N	Weight (g)	Dimension (mm)
436	2	53800029 B	2744.56	D(+)Up.: 51.03
				D(+)Mid.: 50.79
				D(+)Lo.: 50.32
				D(-)Up.: 51.14
				D(-)Mid.: 50.91
				D(-)Lo.: 50.20
				L Up.: 132.75
				L Mid.: 133.06
				L Lo.: 132.10
				H(+): 177
				H(-): 177
Battery S/N	Cell #	Cell S/N	Weight (g)	Dimension (mm)
436	3	53800045 A	2734.47	D(+)Up.: 51.10
				D(+)Mid.: 50.84
				D(+)Lo.: 50.03
				D(-)Up.: 51.09
				D(-)Mid.: 50.78
				D(-)Lo.: 50.04
				L Up.: 133.04
				L Mid.: 133.03
				L Lo.: 132.11



Final Report for 787 Battery (Asset 436) Tested at 70°C, Ungrounded

				H(+): 177
				H(-): 177
Battery S/N	Cell #	Cell S/N	Weight (g)	Dimension (mm)
436	4	53800036 B	2742.20	D(+)Up.: 50.98
				D(+)Mid.: 50.92
				D(+)Lo.: 50.02
				D(-)Up.: 51.06
				D(-)Mid.: 50.76
				D(-)Lo.: 50.10
				L Up.: 133.02
				L Mid.: 133.14
				L Lo.: 132.11
				H(+): 177
				H(-): 177
Battery S/N	Cell #	Cell S/N	Weight (g)	Dimension (mm)
436	5	53800056 A	2747.92	D(+)Up.: 51.21
				D(+)Mid.: 50.85
				D(+)Lo.: 50.15
				D(-)Up.: 51.12
				D(-)Mid.: 50.91
				D(-)Lo.: 50.08
				L Up.: 133.14



Final Report for 787 Battery (Asset 436) Tested at 70°C, Ungrounded

				L Mid.: 133.18
				L Lo.: 132.17
				H(+): 177
				H(-): 177
Battery S/N	Cell #	Cell S/N	Weight (g)	Dimension (mm)
436	6	53800040 B	2736.49	D(+)Up.: 50.95
				D(+)Mid.: 50.82
				D(+)Lo.: 50.02
				D(-)Up.: 51.03
				D(-)Mid.: 50.83
				D(-)Lo.: 50.10
				L Up.: 133.08
				L Mid.: 133.10
				L Lo.: 132.20
				H(+): 178
				H(-): 178
Battery S/N	Cell #	Cell S/N	Weight (g)	Dimension (mm)
436	7	53800057 A	2745.57	D(+)Up.: 51.20
				D(+)Mid.: 50.72
				D(+)Lo.: 50.10
				D(-)Up.: 51.11
				D(-)Mid.: 50.87



Final Report for 787 Battery (Asset 436) Tested at 70°C, Ungrounded

				D(-)Lo.: 50.18
				L Up.: 133.27
				L Mid.: 133.35
				L Lo.: 132.15
				H(+): 177
				H(-): 177
Battery S/N	Cell #	Cell S/N	Weight (g)	Dimension (mm)
436	8	53800066 B	2743.15	D(+)Up.: 51.13
				D(+)Mid.: 50.85
				D(+)Lo.: 49.98
				D(-)Up.: 51.03
				D(-)Mid.: 50.80
				D(-)Lo.: 50.23
				L Up.: 133.02
				L Mid.: 133.06
				L Lo.: 132.15
				H(+): 178
				H(-): 178

APPENDIX C1 – INFRARED SPECTRA FROM ASSET 436 NAIL PENETRATION TEST

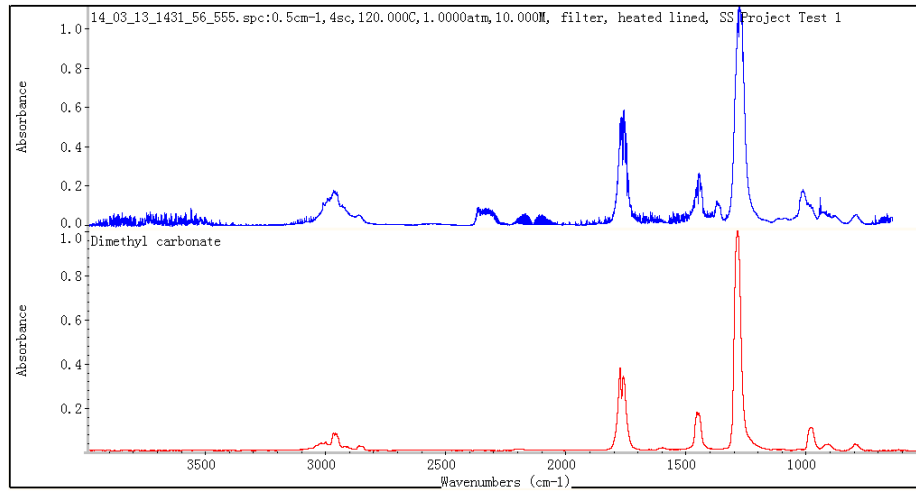


Figure 50. Spectrum of zone A compare to standard spectrum of Dimethyl Carbonate; DMC.

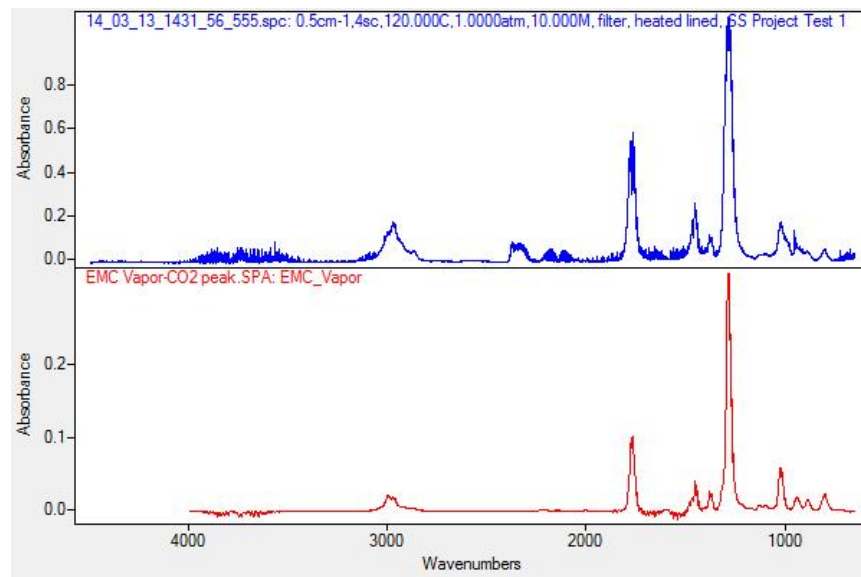


Figure 51. Spectrum of zone A compare to standard spectrum of Ethylmethyl Carbonate; EMC

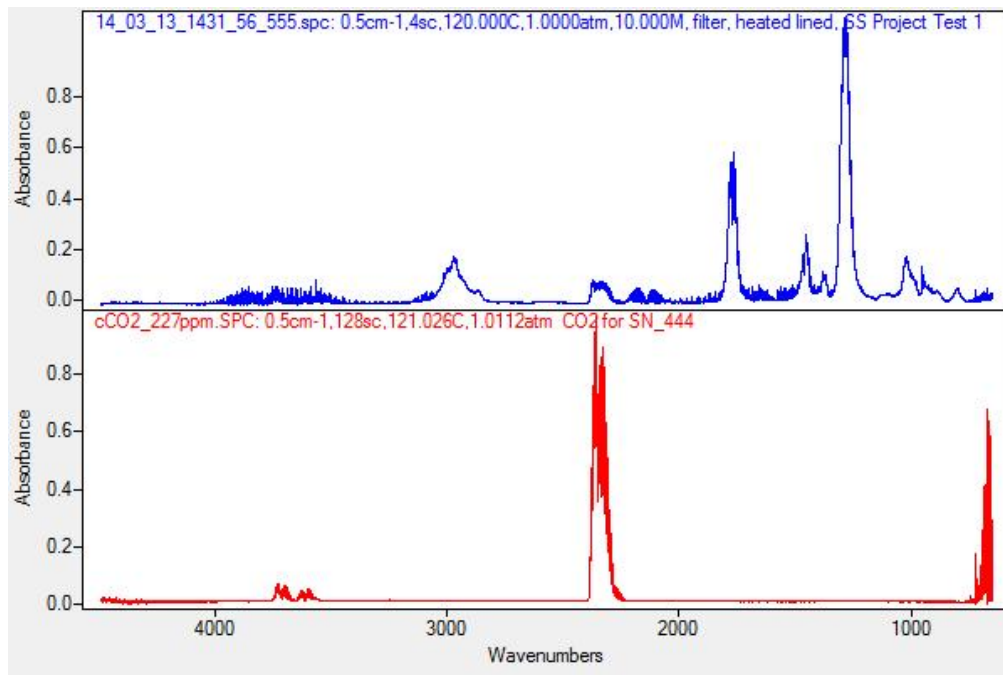


Figure 52. Spectrum of zone A compare to standard spectrum of Carbon dioxide; CO₂.

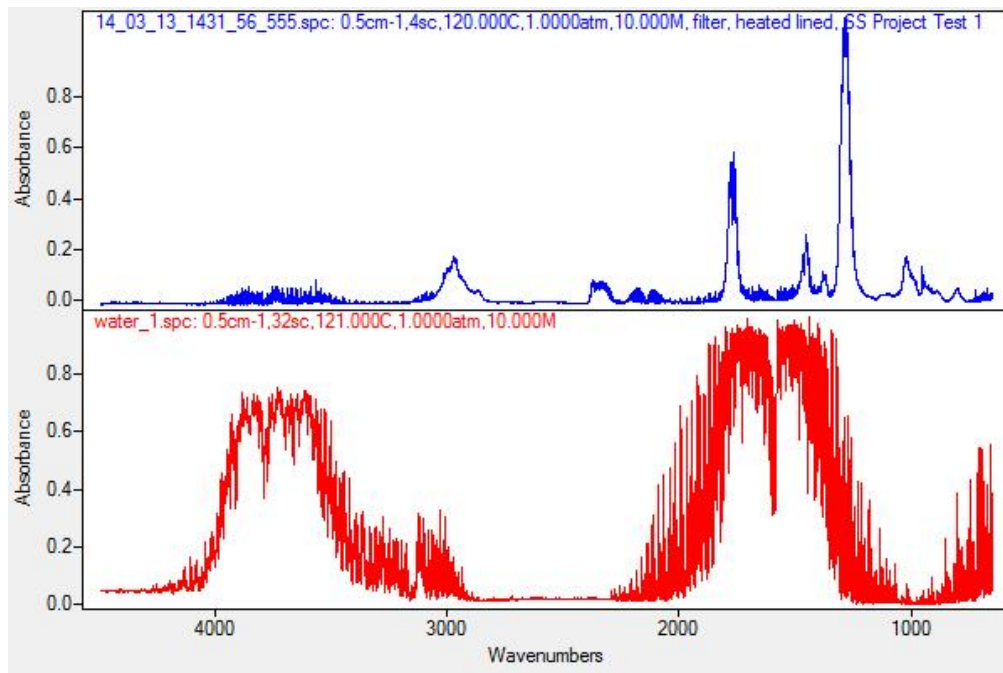


Figure 53. Spectrum of zone A compare to standard spectrum of Water; H₂O.

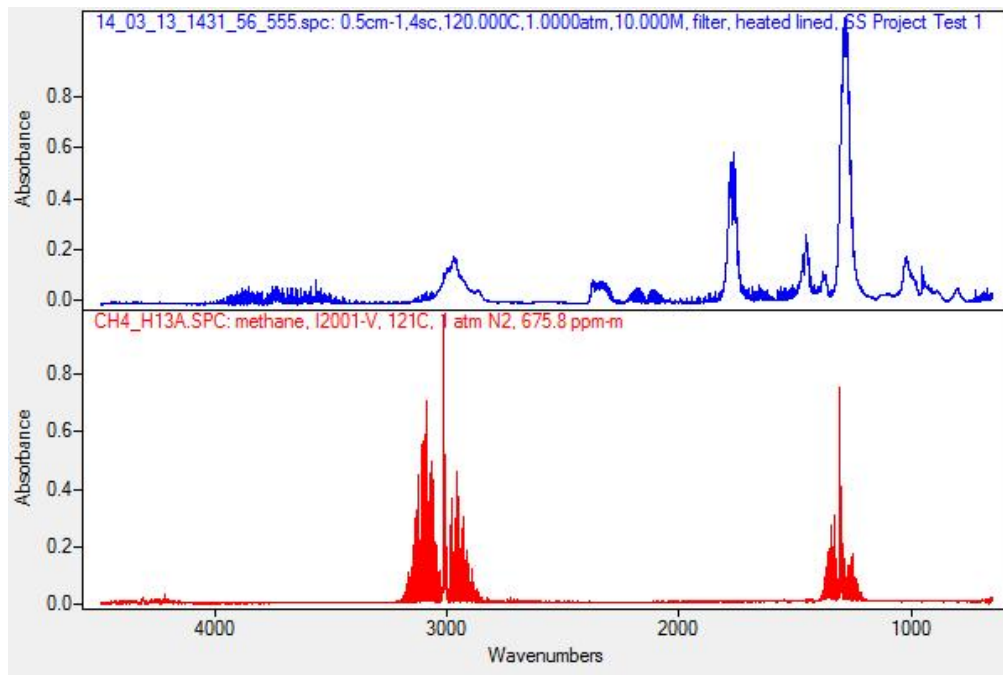


Figure 54. Spectrum of zone A compare to standard spectrum of Methane; CH₄.

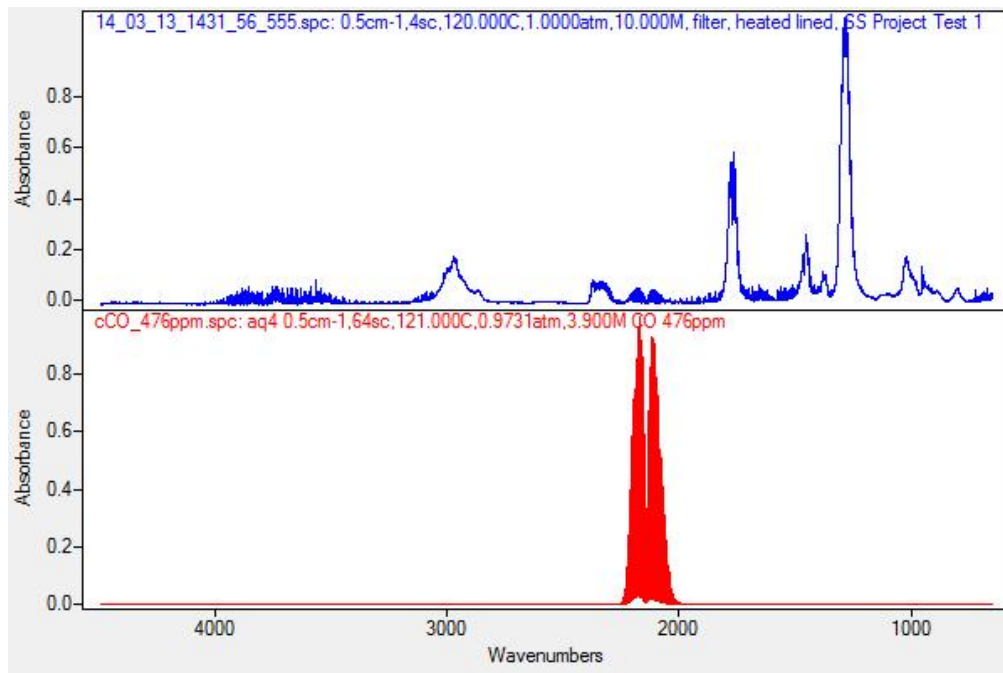


Figure 55. Spectrum of zone A compare to standard spectrum of Carbon mono-oxide; CO.

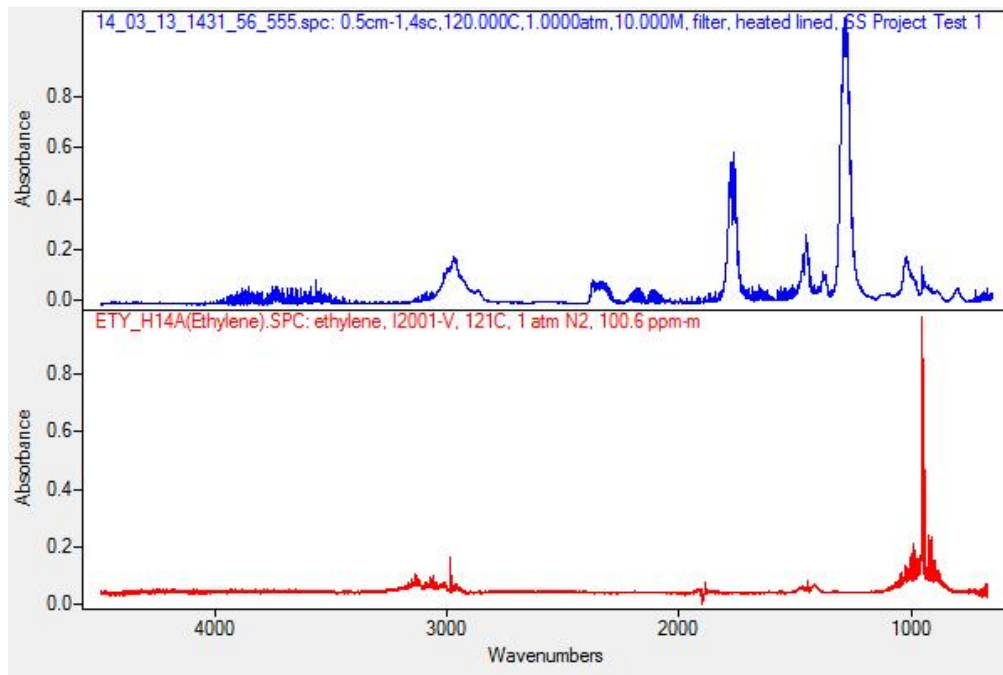


Figure 56. Spectrum of zone A compare to standard spectrum of Ethylene, C_2H_4 .

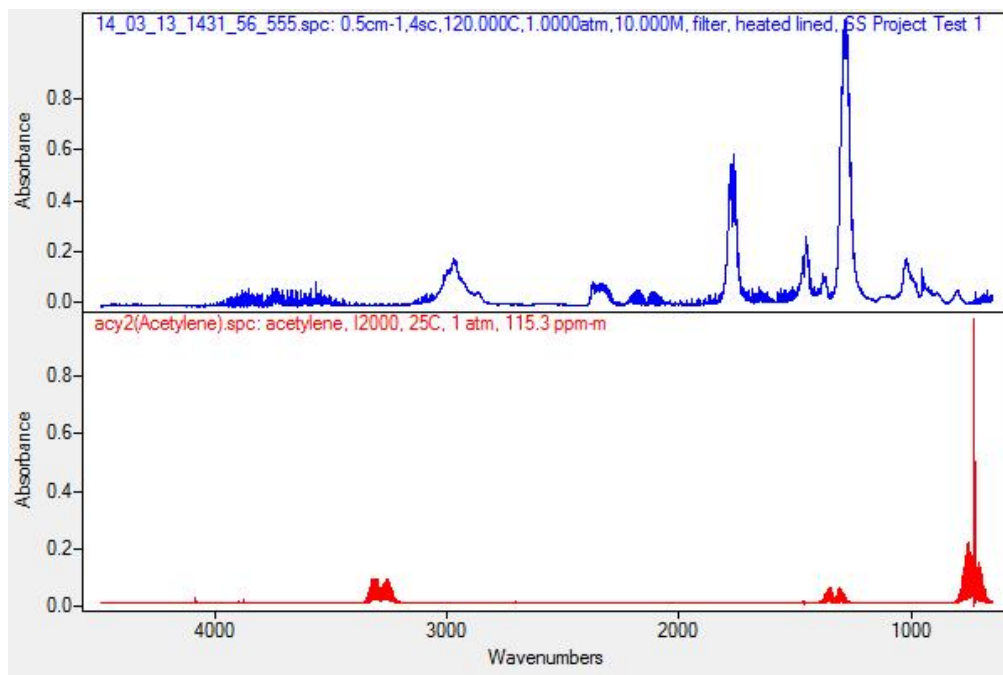


Figure 57. Spectrum of zone A compare to standard spectrum of Acetylene, C_2H_2 .

APPENDIX C2 – INFRARED SPECTRA FROM ASSET 436 NAIL PENETRATION TEST

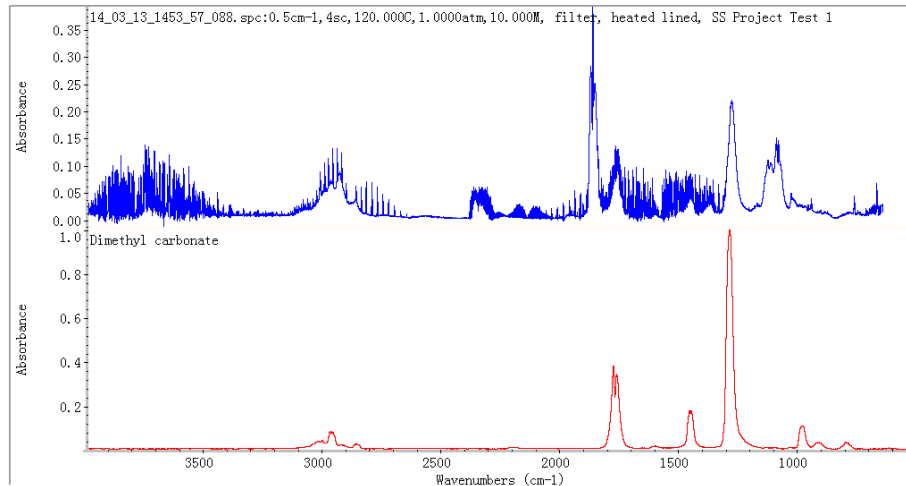


Figure 58. Spectrum of zone D compare to standard spectrum of Dimethyl Carbonate; DMC.

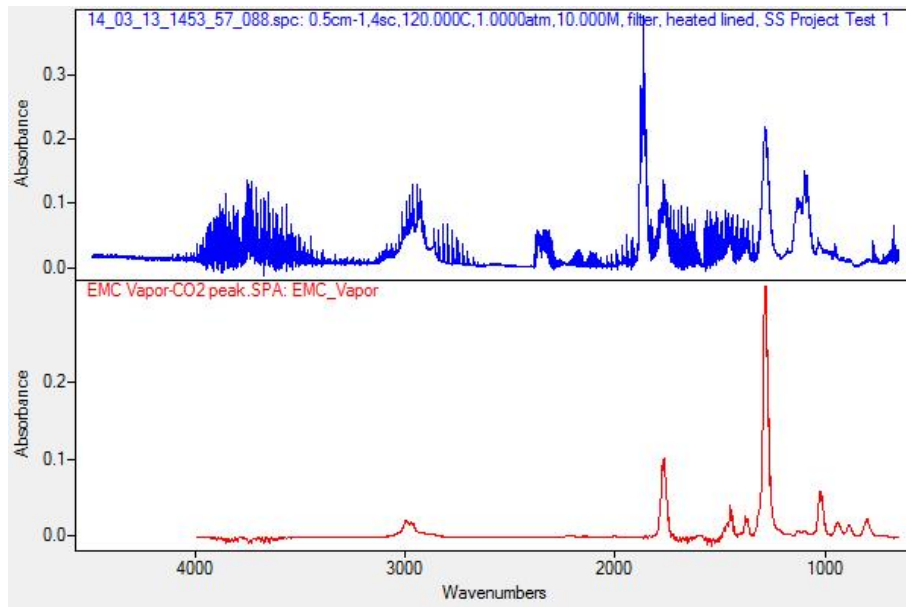


Figure 59. Spectrum of zone D compare to standard spectrum of Ethylmethyl Carbonate; EMC

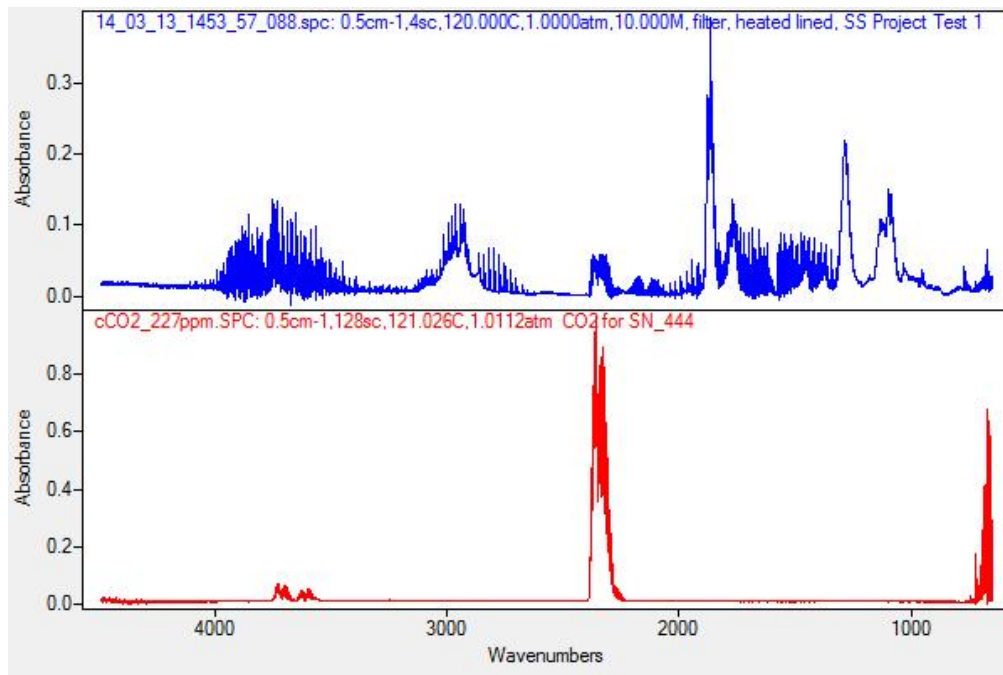


Figure 60. Spectrum of zone D compare to standard spectrum of Carbon dioxide; CO₂.

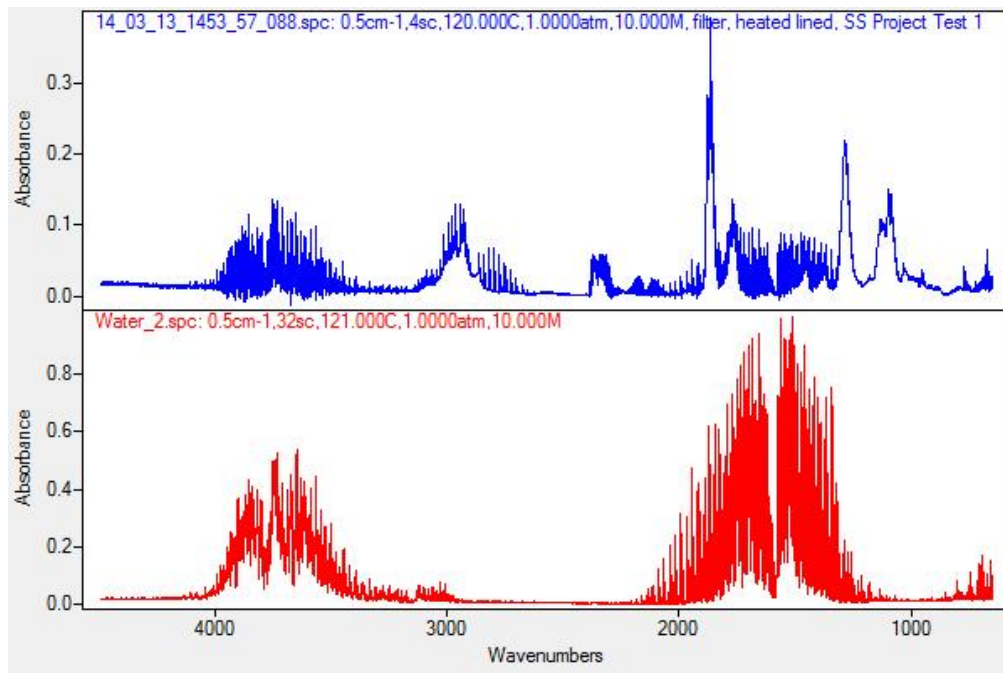


Figure 61. Spectrum of zone D compare to standard spectrum of Water; H₂O.

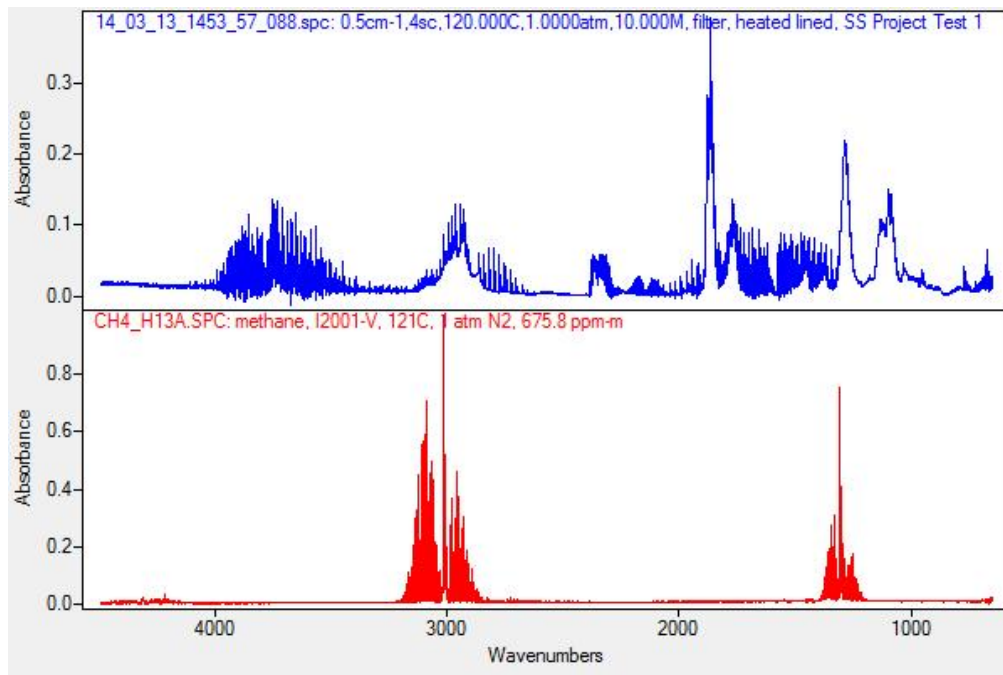


Figure 62. Spectrum of zone D compare to standard spectrum of Methane; CH₄.

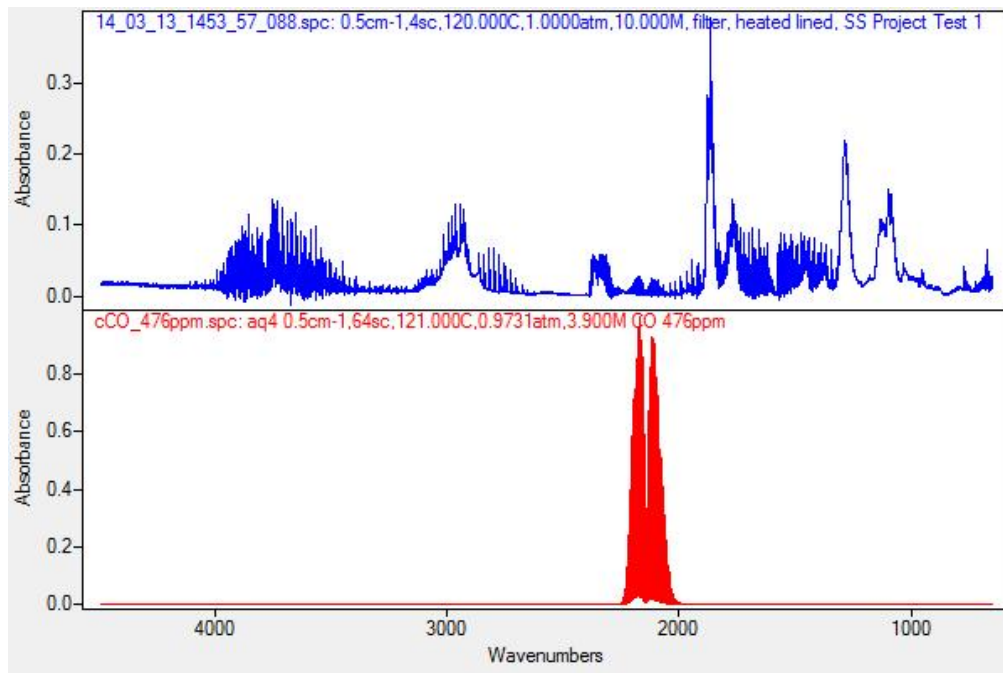


Figure 63. Spectrum of zone D compare to standard spectrum of Carbon mono-oxide; CO.

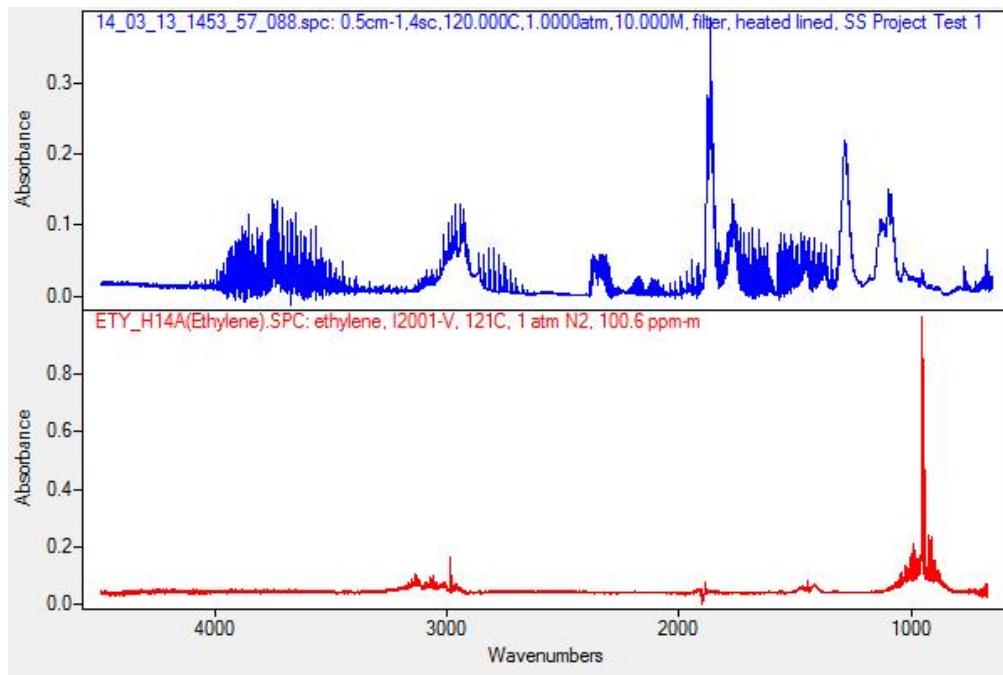


Figure 64. Spectrum of zone D compare to standard spectrum of Ethylene, C_2H_4 .

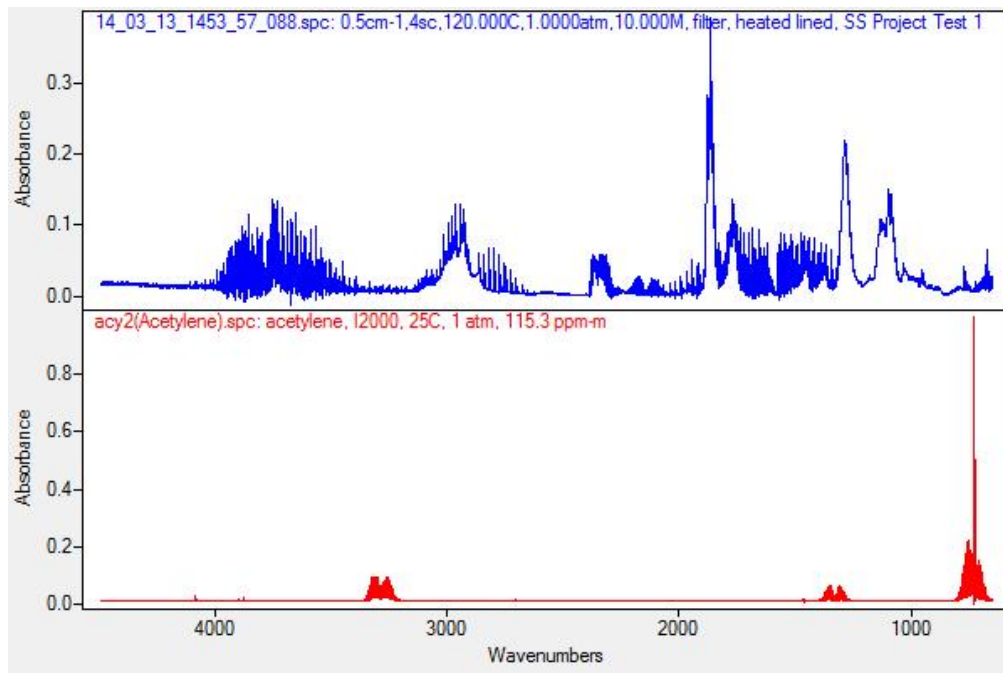


Figure 65. Spectrum of zone D compare to standard spectrum of Acetylene, C_2H_2 .

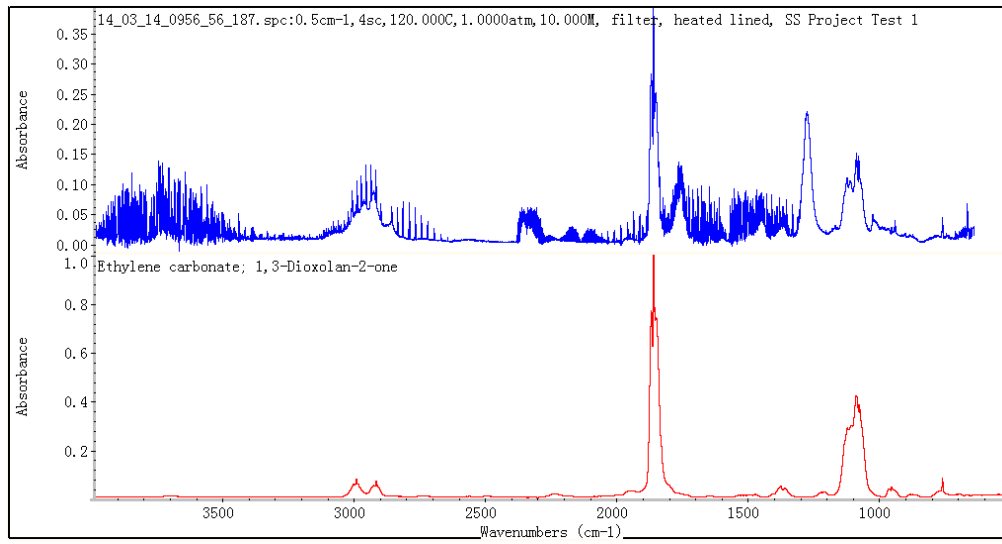


Figure 66. Spectrum of zone D compare to standard spectrum of Ethylene Carbonate; EC.

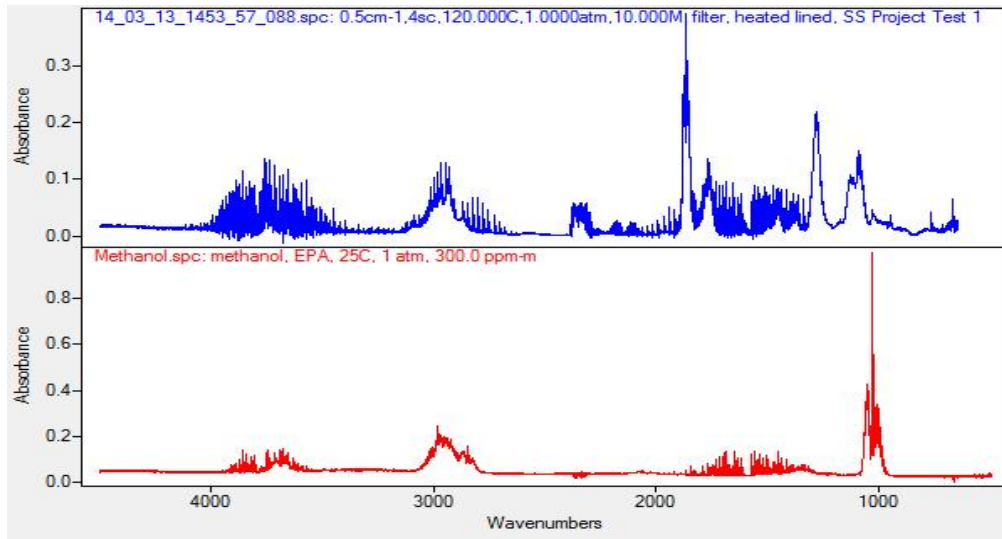


Figure 67. Spectrum of zone D compare to standard spectrum of Methanol; CH₃OH.

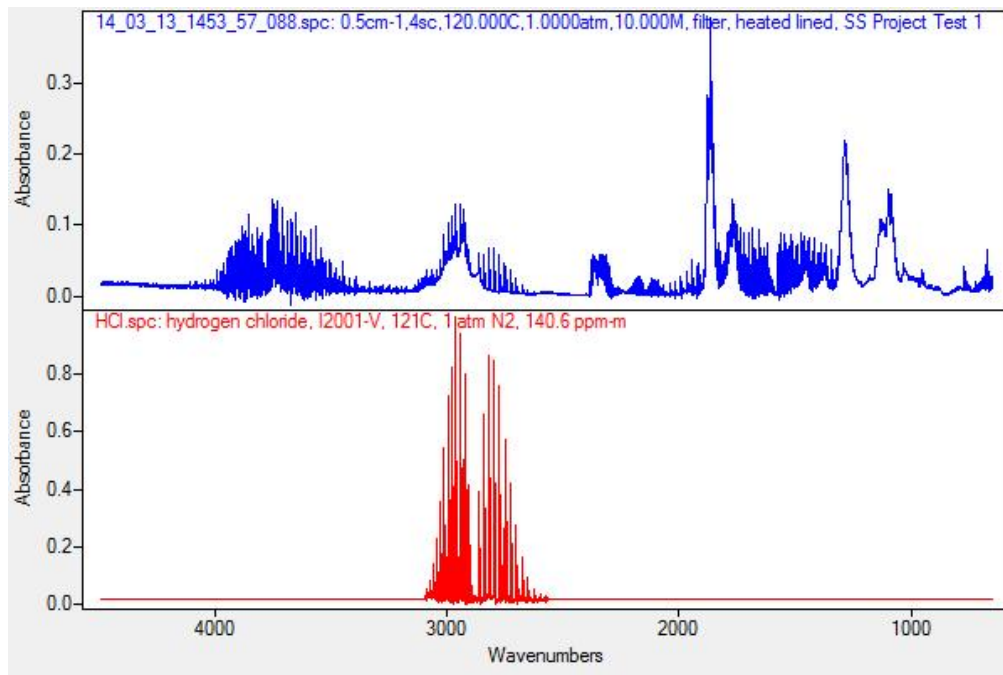


Figure 68. Spectrum of zone D compare to standard spectrum of Hydrogen Chloride; HCl.

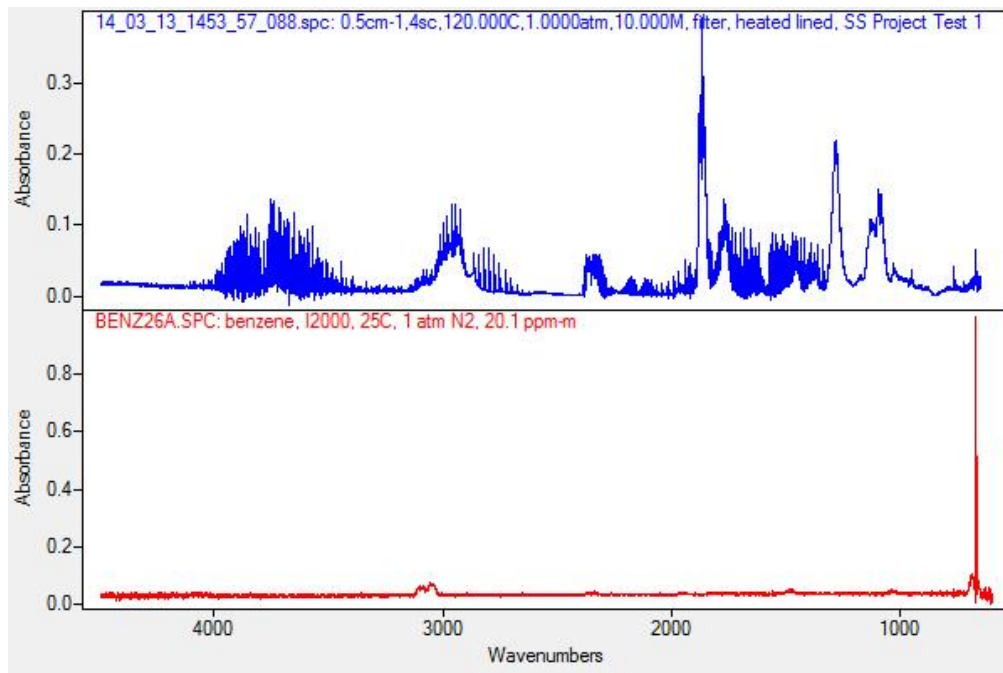


Figure 69. Spectrum of zone D compare to standard spectrum of Benzene; C₆H₆.